NASA Contractor Report 187512

ICASE Report No. 91-10

ICASE

DEVELOPMENT OF THE WAKE BEHIND A CIRCULAR CYLINDER IMPULSIVELY STARTED INTO ROTATORY AND RECTILINEAR MOTION: INTERMEDIATE ROTATION RATES

Yen-Ming Chen
Yuh-Roung Ou
Arne J. Pearlstein

NASA

National Aeronautics and
Space Administration

Langley Research Center
Hampton, Virginia 23665-5225

Development of the Wake behind a Circular Cylinder Impulsively Started into Rotatory and Rectilinear Motion: Intermediate Rotation Rates

Yen-Ming Chen[1]
NASA-Langley Research Center
Hampton, VA 23665

Yuh-Roung Ou[2]
Institute for Computer Applications in Science and Engineering
NASA-Langley Research Center
Hampton, VA 23665

Arne J. Pearlstein[3]
Department of Mechanical and Industrial Engineering
University of Illinois at Urbana-Champaign
1206 West Green Street
Urbana, IL 61801

ABSTRACT

The temporal development of two-dimensional viscous incompressible flow generated by a circular cylinder started impulsively into steady rotatory and rectilinear motion is studied by integration of a velocity/vorticity formulation of the governing equations, using an explicit finite-difference/pseudo-spectral technique and a new implementation of the Biot-Savart law. Results are presented for a Reynolds number of 200 (based on the cylinder diameter $2a$ and the magnitude U of the rectilinear velocity) for several values of the angular/rectilinear speed ratio $\alpha = \Omega a/U$ (where Ω is the angular speed) up to 3.25. For values of $\alpha \le 1$, our extension of the computations to larger dimensionless times than those possible in the experimental work of Coutanceau & Ménard (1985) or considered in the computational work of Badr & Dennis (1985) allows for a more complete discussion of the long-term development of the wake. We also discuss several aspects of the kinematics and dynamics of the flow not considered earlier. For higher values of α, our results indicate that for $Re = 200$, vortex shedding does indeed occur for $\alpha = 3.25$ (and possibly for higher values of α also), in contrast to the conclusion of Coutanceau & Ménard (1985). The shedding process is, however, very different from that which gives rise to the usual Kármán vortex street for $\alpha = 0$. In particular, consecutive vortices shed by the body can be shed from the same side, and be of the same sense, in contrast to the nonrotating case, in which mirror-image vortices of opposite sense are shed alternately on opposite sides of the body. The implications of the results are discussed in relation to the possibility of suppressing vortex shedding by open- or closed-loop control of the rotation rate.

1. Introduction

Flow past a rotating circular cylinder is a prototypical problem in the study of unsteady flow separation (Telionis 1981). It is also of considerable practical importance in boundary layer control on airfoils (cf. Tennant et al. 1976 and Modi et al. 1990), and in lift enhancement schemes employing the Magnus effect (Swanson 1961). Rotating all or part of a body may also have applications in active or feedback control of vortex shedding, with important consequences for wake modification and the reduction of flow-induced vibration.

In this work, we describe a study of the development of the two-dimensional flow generated by a circular cylinder of radius a started impulsively into a combined steady rotatory and rectilinear motion, with angular speed Ω about its axis and rectilinear speed U normal to its generators. The fluid is taken to be at rest initially. The two parameters governing the development of the flow are the Reynolds number, defined by $Re = 2aU/\nu$, where ν is the kinematic viscosity, and the ratio of rotatory to rectilinear speeds, defined by $\alpha = \Omega a/U$.

Experimental studies of the nominally two-dimensional flow past a circular cylinder undergoing steady rotatory and rectilinear motion have been conducted by Prandtl (Prandtl 1925, Prandtl & Tietjens 1934), Taneda (1977, 1980), Koromilas & Telionis (1980), Díaz et al. (1983), Werlé (1984), and most extensively by Coutanceau & Ménard (1985). An excellent summary of earlier work has been provided by the latter authors, to whose paper the reader is referred. On the basis of their experiments (primarily at Re = 200, but including results for Re as high as 1000), Coutanceau & Ménard concluded that a (modified) Kármán vortex street

1

"disappears completely for α greater than a certain limiting value α_L. The value of α_L has been found to be not very dependent on the Reynolds number and to be about 2. For $\alpha > \alpha_L$ no other eddy is created after E_1(the first eddy formed) during the time of the observations, so that the eddy street must have been destroyed."

They found this conclusion to be consistent with the earlier experimental work by Prandtl, Díaz et al., and Werlé and proposed, as a simple physical explanation for the disappearance of the Kármán vortex street at high values of α, that

"for low values of α, eddies would be alternately shed on each side of the cylinder to form a Bénard-Kármán street, as for the pure translation ($\alpha = 0$). But the eddies on the side moving in the direction of the rotation decrease progressively when α increases and then disappear completely. Thus it was found that the Bénard-Kármán structure begins to deteriorate as soon as the peripheral velocity becomes greater than the free-stream velocity (giving rise to a zigzag oscillating wake) and finally disappears for $\alpha > 2.5$."

When one examines the evidence for these statements, one finds that it is not overly strong, particularly for the critical value of α and its dependence on *Re*. For *Re* = 9000 and several values of α, Díaz et al. (1983) made hot-wire measurements of the streamwise velocity, and computed its autocorrelation. They found that for $\alpha = 0$ and $\alpha = 1$, the velocity autocorrelations were very similar, approximately periodic, and had local maxima separated by a time corresponding to the nominal Strouhal frequency. For $\alpha = 1.5$ and $\alpha = 2$, the autocorrelation function was progressively reduced. Díaz et al. (1983) did indeed conclude that "for peripheral velocities up to

2

the value of the free-stream velocity, a distinct Kármán vortex activity exists within the wake, whereas for greater peripheral velocities, the Kármán activity deteriorates and disappears for values in excess of twice the free-stream velocity.'' On the other hand, for $Re \approx 3300$, Werlé (1984) noted that for values of α in excess of that at which separation is eliminated, ''when the tangential velocity increases further, the cylinder finally entrains an entire layer of relatively turbulent fluid in its rotation. More or less periodic instabilities then appear.'' From this, it is not clear whether vortex shedding is really suppressed by rotation at $Re \approx 3300$. At still lower Re, we note that the experiments of Coutanceau & Ménard (1985) were preformed in a towing tank, which allowed observations to be made over only a very limited range of dimensionless time.

The issues of whether the Kármán vortex street is destroyed and vortex shedding is suppressed are of considerable practical interest from the standpoint of wake modification and the reduction of flow-induced vibration. In particular, it is of interest to determine whether for a given Re, there is a value of α_L beyond which vortex shedding disappears. An additional factor tending to complicate the experimental resolution of these issues is that in either a fixed reference frame or one translating with the cylinder, the generation and shedding of vortices might be masked (Perry, Chong & Lim, 1982) at large values of α by the high velocities induced in the near wake by the rapidly rotating cylinder. The presence of a vortex in this flow would be most conveniently determined from a reference frame moving with the vortex, which is more easily accomplished by theoretical work than in an experiment.

To date, however, most of the theoretical studies have shed no light on the question of whether cylinder rotation can suppress vortex shedding. The analytical investigations of flow past a rotating and translating circular cylinder (Glauert 1957a,

3

1957b, Moore 1957, and Wood 1957) are based on steady boundary layer theory, and are hence inapplicable to the investigation of the unsteady separated flow associated with vortex shedding. The computational investigations of the flow generated by a rotating and translating cylinder reported by Ta Phuoc Loc (1975), Lyulka (1977), Townsend (1980), Ingham (1983) and Ingham & Tang (1990) concern only the steady flow with $Re \leq 30$. Although Shkadova (1982) discussed a computational algorithm for the unsteady flow, she presented only a single set of streamlines for each of four combinations of Re and α (Re = 20, 40, and 80 for α = 0.2, and Re = 40 for α = 3). She did not discuss unsteady effects for the case of a rotating and translating cylinder, and it is not clear whether the streamlines presented for each combination of Re and α pertained to a computed steady flow, or to instantaneous streamlines (at unspecified times) in an unsteady flow. In the earlier work of Simuni (1967) concerning the flow generated by a cylinder accelerated smoothly (rather than impulsively) into rotatory and rectilinear motion, the time-dependence of the body motion was not clearly specified, nor was any information provided about the time-dependence of the computed solution.

To the best of our knowledge, the only investigations of vortex shedding by a steadily rotating and translating circular cylinder in the laminar regime besides the experimental work of Coutanceau & Ménard (1985) are the computational investigations of Badr & Dennis (1985) and Badr, Dennis & Young (1989), both of which were conducted in conjunction with those experiments. Although these investigators realized the importance of extending the computations to larger α, their work was limited to $\alpha \leq 1$, and so shed no light on the conclusion of Coutanceau Ménard (1985) cited above.

In the present work, for Re = 200, we present computations extending the range

of α to the highest value (3.25) studied experimentally by Coutanceau & Ménard (1985). After comparing our results at lower values of α to the previous work of Coutanceau & Ménard (1985) and Badr & Dennis (1985), we present results for the two largest values of α (2.07 and 3.25) considered by the former authors. Ours is the first computational investigation at $Re = 200$ for $\alpha > 1$, and is significant in light of the earlier conclusions that vortex shedding is suppressed for $\alpha > 1$ or $\alpha > 2.5$. Our computed results are in excellent agreement with the experiments of Coutanceau & Ménard (1985) for $Re = 200$ and $\alpha = 2.07$. We then present strong evidence in support of the hypothesis that rotation does not suppress vortex shedding for $Re = 200$ and $\alpha = 3.25$. This evidence, consisting of streamlines viewed from a reference frame moving with a vortex, and of contours of constant vorticity, is of a type not easily obtainable in the laboratory, and provides an important demonstration of the capability of computational methods to resolve questions that arise from experiment.

In §2, we present the governing equations, along with a transformed version appropriate for computations with a body-fitted time-dependent grid used in the computations at $\alpha = 3.25$. In §3, we briefly describe the numerical methods employed, including a new implementation of the Biot-Savart law used to satisfy boundary conditions on the vorticity at the cylinder and on the velocity in the far field. Section 4 discusses a technique more general than that employed in earlier studies for determining the initial flow (at $t = 0^+$). The main results, including comparisons to the experiments of Coutanceau & Ménard (1985) and discussion of features of the flow not elucidated by their work or earlier computations, are presented in §5, followed by our conclusions in §6.

2. Governing equations

A nonrotating reference frame translating with the cylinder is used in this study. In this frame, the fluid at infinity has a uniform velocity of magnitude U in the x-direction, and the cylinder rotates in the counterclockwise direction with angular velocity Ω, as shown in figure 1.

The motion of an incompressible viscous fluid is governed by the continuity and momentum equations. A velocity/vorticity formulation, consisting of the vorticity transport equation and a vector Poisson equation for velocity, is used in this study. In two dimensions, the dimensionless equations are (Wu 1975; Fasel 1976):

$$\frac{\partial \omega}{\partial t} + \vec{V} \cdot \nabla \omega = \frac{2}{Re} \nabla^2 \omega \qquad (1)$$

and

$$\nabla^2 \vec{V} = -\nabla \times (\omega \vec{e}_z) \qquad (2)$$

where we use the cylinder radius a as the length scale, and a/U as the time scale. The velocity is normalized by the uniform translational speed U. Equation (2) is derived from the continuity equation

$$\nabla \cdot \vec{V} = 0, \qquad (3)$$

the definition of vorticity for a two-dimensional flow

$$\omega \vec{e}_z = \nabla \times \vec{V}, \qquad (4)$$

and the vector identity

$$\nabla \times \nabla \times \vec{V} = \nabla\left(\nabla \cdot \vec{V}\right) - \nabla^2 \vec{V}. \tag{5}$$

The dimensionless boundary conditions are

$$\vec{V} = \vec{e}_x \qquad \text{at infinity} \tag{6}$$

$$\vec{V} = -\alpha \sin\theta\, \vec{e}_x + \alpha \cos\theta\, \vec{e}_y \quad \text{on the cylinder surface.} \tag{7}$$

To allow for computation of the flow on a time-dependent grid, we write the components of (1) and (2) in general body-fitted (ξ, η) coordinates as

$$\begin{aligned}
\omega_t = &\frac{x_t}{J}\left(\omega_\xi y_\eta - \omega_\eta y_\xi\right) - \frac{y_t}{J}\left(\omega_\xi x_\eta - \omega_\eta x_\xi\right) \\
&- \frac{1}{J}\left[y_\eta(u\omega)_\xi - y_\xi(u\omega)_\eta + x_\eta(v\omega)_\xi - x_\xi(v\omega)_\eta \right] \\
&+ \frac{2}{ReJ^2}\left(\alpha\omega_{\xi\xi} - 2\beta\omega_{\xi\eta} + \gamma\omega_{\eta\eta}\right) + \frac{2}{Re}\left(P\omega_\xi + Q\omega_\eta\right),
\end{aligned} \tag{8}$$

and

$$\alpha u_{\xi\xi} - 2\beta u_{\xi\eta} + \gamma u_{\eta\eta} + J^2\left(Pu_\xi + Qu_\eta\right) = J\left(x_\eta\omega_\xi - x_\xi\omega_\eta\right), \tag{9}$$

and

$$\alpha v_{\xi\xi} - 2\beta v_{\xi\eta} + \gamma v_{\eta\eta} + J^2\left(Pv_\xi + Qv_\eta\right) = J\left(y_\eta\omega_\xi - y_\xi\omega_\eta\right) \tag{10}$$

(Reddy & Thompson 1977) where

$$\alpha = x_\eta^2 + y_\eta^2,$$

$$\beta = x_\xi x_\eta + y_\xi y_\eta,$$

$$\gamma = x_\xi^2 + y_\xi^2, \tag{11}$$

$$P = \xi_{xx} + \xi_{yy},$$

$$Q = \eta_{xx} + \eta_{yy},$$

and

$$J = x_\xi y_\eta - x_\eta y_\xi \tag{12}$$

is the Jacobian of the mapping between the (x, y) and (ξ, η) coordinate systems. Here, subscripts denote partial differentiation. In (8) and in the computer code developed, we have allowed the grid in the physical (x, y) space to be time-dependent. This introduces additional terms associated with x_t and y_t into the governing equations in the generalized coordinate system. In this study, the body-fitted grid is simply one of cylindrical polar coordinates and is time-independent, except for $\alpha = 3.25$ where the grid is made time-dependent for the calculation between $t = 24$ and 54. The grid is uniformly spaced in the circumferential direction and is stretched in the radial direction, as described below.

3. Numerical methods

In numerical simulations, it is necessary to confine the computation to a finite domain. As a result, (6) cannot be directly applied at the outer perimeter of the computational domain. Various far-field boundary conditions, including those derived from potential flow and Oseen expansions, have been adopted in the past. The conditions imposed at the outer perimeter of the computational domain have

8

been found to strongly influence the accuracy of computations of steady flows in this unbounded geometry (Fornberg 1980; Ingham 1983; Ingham & Tang 1990). A second difficulty, common to most simulations based on primitive variable (pressure/velocity) or velocity/vorticity formulations is the fact that conditions on either the vorticity or pressure are required at solid boundaries. In this work, both of these difficulties are resolved by use of a new implementation of the Biot-Savart law briefly described below. For further details, the reader is referred to the work of Wu and coworkers (Wu & Thompson 1973; Wu 1976; Wang & Wu 1986), and Chen & Pearlstein (1991).

The definition (4) allows determination of the vorticity field from a known velocity field. Conversely, one can determine the velocity field from a known vorticity field *via* the generalized Biot-Savart law, which in two dimensions can be written as

$$
\begin{aligned}
\vec{V}(\vec{r}_0, t) = &- \frac{1}{2\pi} \int \int_D \frac{\vec{\omega}(\vec{r}, t) \times (\vec{r} - \vec{r}_0)}{|\vec{r} - \vec{r}_0|^2} dA \\
&- \frac{1}{2\pi} \int \int_B \frac{2\vec{\Omega}(\vec{r}, t) \times (\vec{r} - \vec{r}_0)}{|\vec{r} - \vec{r}_0|^2} dA + \vec{V}_\infty
\end{aligned}
\tag{13}
$$

(Wu 1976), where the subscript 0 denotes the field point where the velocity is evaluated, and $\vec{V}_\infty$ is the uniform flow at infinity. The first integral in (13) is evaluated numerically over the fluid domain D, while the second integral is evaluated analytically over the solid body B. Here, $\vec{\omega} = \omega \vec{e}_z$ is the vorticity at a point within the fluid, and $\vec{\Omega} = \Omega \vec{e}_z$ is the angular velocity of a point within B.

Equation (13) serves two purposes in this study. First, if the vorticity field $\vec{\omega}(\vec{r}, t)$ is known and the domain D is large enough to contain all of the vorticity generated at the solid boundary prior to time t, then the velocity on the perimeter of D can be evaluated directly by numerical integration of (13). Second, by linking the velocity

and vorticity fields, (13) provides a basis for determining the vorticity on the solid boundary. Applying (13) to points $\vec{r}_b$ on the solid boundary, one obtains

$$
\vec{V}(\vec{r}_b, t) = -\frac{1}{2\pi} \int\int_D \frac{\vec{\omega}(\vec{r}, t) \times (\vec{r} - \vec{r}_b)}{|\vec{r} - \vec{r}_b|^2} \, dA
$$
$$
-\frac{1}{2\pi} \int\int_B \frac{2\vec{\Omega}(\vec{r}, t) \times (\vec{r} - \vec{r}_b)}{|\vec{r} - \vec{r}_b|^2} \, dA + \vec{V}_\infty.
$$
$$(14)$$

If $\vec{V}_\infty$ and the body motion $\vec{V}(\vec{r}_b, t)$ and $\vec{\Omega}$ are given, and the vorticity is known everywhere except on the solid boundary, then the only unknowns in (14) are the vorticity values on the solid boundary. Therefore, one can solve (14) as a vector Fredholm integral equation of the first kind to obtain the vorticity values at grid points on the solid boundary.

In this work, the numerical integration of (13) and (14) is performed over each quadrilateral element in D using isoparametric representations commonly used in the finite element method. All variables are located at the intersections of grid lines, namely, corners of quadrilateral elements. The vorticity distribution over each quadrilateral element is approximated by bilinear shape functions. Integration is then performed over the [-1, 1] × [-1, 1] square in the isoparametric plane. When the field point is far from the quadrilateral element, more efficient asymptotic formulas (Weston & Liu 1982; Ting 1983) are employed. Further details are provided in Chen (1989).

In deriving the discretized forms of (8)–(10), second-order central differences are used for all derivatives in the radial direction η, while a pseudo-spectral transform method (Orszag 1980; Zang et al. 1982) is used to evaluate all derivatives in the circumferential direction ξ. The cross-derivative terms are approximated by central differencing in η followed by pseudo-spectral transformation in ξ. We use a fully

explicit method to advance the vorticity transport equation (8) in time to obtain the vorticity values at the interior grid points. The vorticity on the outer perimeter of the computational domain is obtained by extrapolation. At this stage, the vorticity on the solid boundary lags by one time step. If this vorticity field were used to evaluate the right hand side of (14), the result would not satisfy the no-slip and no-penetration conditions. The continuous generation of vorticity at the cylinder is properly simulated in our computations by adding or subtracting vorticity at the boundary at each time level in order to satisfy (14) identically.

It should be noted that the solution to (14) is not unique (Wu 1976; Taslim et al. 1984). To render the solution unique, Wu (1976) developed and imposed the principle of vorticity conservation, which states that the total vorticity in the combined fluid and solid regions must be zero at all times. A more general and robust procedure, applicable to flows over single and multiple solid bodies, has been developed by Chen & Pearlstein (1991), and is used here.

The computational loop to advance the solution from one time level to the next consists of the following steps:

1. The discretized vorticity transport equation (8) is advanced explicitly to obtain new vorticity values at all interior grid points, using a second-order rational Runge-Kutta method (Wambecq 1978). In contrast to the three-step Adams-Bashforth method used by previous authors, this allows a much larger time-step size due to a less severe stability constraint.

2. Using known vorticity values at the interior grid points, the kinematic constraint (14) is used to update the vorticity values on the solid boundary.

3. Using the updated vorticity field, the velocity at points on the outer perimeter of

the computational domain is evaluated by (13). Once velocity boundary values are known, Poisson equations (9) and (10) are solved for the new velocity field. The discretizations of (9) and (10) are 11-banded and block-diagonal in form, and are solved by a preconditioned biconjugate gradient routine (Chen et al. 1989).

The method outlined above is particularly well suited for the initial development of the flow generated by impulsively started bodies. This is because the vorticity is initially concentrated near the solid body. Therefore, the numerical simulation can be confined to a domain within which all vorticity is contained. Since the velocity at the outer perimeter of the computational domain is calculated *via* (13), imposition of computational far-field velocity boundary conditions is avoided. The use of (13) in calculating the far-field velocity is numerically exact at time t if the computational domain is large enough to contain all vorticity generated at the cylinder surface prior to t. We note that, in the streamfunction/vorticity formulation, the streamfunction values on the outer perimeter of the computational domain can be obtained similarly by using an integral constraint equation (Wu & Sampath 1976). We also note that the velocity field can be obtained by applying (13) at every grid point. This results in a point-by-point scheme which, unlike schemes using the Poisson equations (9) and (10), does not require solution of large linear equation systems. This approach was adopted in Wu's earlier work, and might be attractive on massively parallel computers.

The size of the computational domain is chosen according to the time span investigated. Here, we set the outer boundary of the computational domain to be a circle of radius 24 for $t \leq 24$. We use 128 uniformly spaced and 120 stretched grid lines in the θ- and r-directions, respectively. The stretching function of Vinokur (1983) is used to distribute the circular grid lines on $1 \leq r \leq 24$. The stretching function allows grid points to be clustered near one or both ends of the domain, or

anywhere between them, by adjusting two parameters s_0 and s_1. Here, s_0 and s_1 are the ratios of the spacing if N points were distributed uniformly, to the spacings at the inner and outer boundaries, respectively. For $\alpha = 0.5$ and 1, we set $s_0 = 5.0$ and $s_1 = 0.25$. The grid spacings adjacent to the cylinder and at the outer perimeter are 4% and 75% of the cylinder radius, respectively. For $\alpha = 2.07$ and 3.25, we set $s_0 = 10.0$ and $s_1 = 0.25$ to further cluster circular grid lines near the cylinder, with grid spacings adjacent to the cylinder and at the outer perimeter being 2% and 76% of the cylinder radius, respectively. At the end of the simulation, the magnitude of vorticity on the outer perimeter is less than 10^{-5} for all cases except as noted, indicating that only a negligible amount of vorticity has escaped the domain.

4. Determination of the initial flow

In most numerical simulations of flow over impulsively started bodies, the initial flow field is taken to be the potential flow, since the vorticity at $t = 0^+$ is concentrated on the body surface in the form of a vortex sheet. Perturbation solutions in which t is the small parameter have also been used as initial conditions (Collins & Dennis 1973 for $\alpha = 0$; Badr & Dennis 1985 for $\alpha \neq 0$). Both approaches require special techniques in order to obtain the initial flow field. In the present work, determination of the initial flow field requires no special treatment. The same procedure used for determining the boundary vorticity distribution satisfying the no-slip and no-penetration conditions is applied. More specifically, (14) is solved for the unknown boundary vorticity at $t = 0^+$, with the vorticity taken to be zero at every grid point away from the cylinder surface. Once the boundary vorticity values are obtained, the initial velocity field is determined by solving (9) and (10), with the velocity on the outer perimeter of the computational domain determined by application of (13) to points on the outer

perimeter. This versatile procedure enables the numerical code to handle bodies of arbitrary shape undergoing arbitrary rotational and translational motion.

Errors in approximating the vorticity layer of infinitesimal thickness at $t = 0^+$ are inherent to any computational scheme. However, as discussed by Lugt & Haussling (1974), even in the worst case of a body set impulsively into motion, the duration of these errors is confined to a very limited time close to $t = 0$. For the present algorithm, this will be confirmed in §5 by comparison of our numerical results to the perturbation solution of Badr & Dennis (1985) at small times.

5. Results and discussion

In this section, numerical results for $Re = 200$ with $\alpha = 0.5$, 1, 2.07, and 3.25 are presented and discussed. The parameter values chosen allow comparison to the experimental results of Coutanceau & Ménard (1985) and permit a critical evaluation of their conclusions regarding the suppression of vortex shedding by rotation. For $\alpha = 0.5$ and 1, excellent agreement with the experimental (Coutanceau & Ménard 1985) and numerical (Badr & Dennis 1985) results is obtained. For $\alpha = 2.07$, for which no numerical results have been previously reported, we obtain excellent agreement with experiment. For $\alpha = 3.25$, the relatively small disagreement between experiment and our computations is probably due to three-dimensional effects in the former (see §5.4). For all cases investigated, we continue the simulations to larger dimensionless times ($t \geq 24$) than could be studied experimentally by Coutanceau & Ménard (1985), so that the nature of the long-time solution can be better discerned. For $\alpha = 3.25$, we further extend our calculation to $t = 54$ to include shedding of the second and third vortices. We note that the time scale adopted here is the same as that used by Badr & Dennis (1985). Conversion of our dimensionless times to those reported by

Coutanceau & Ménard (1985) requires multiplication of the latter by a factor of two.

As discussed in §4, the solution procedure presented in §3 is applied at $t = 0^+$ to obtain the initial flow field. Errors are present due to the inability of any numerical scheme to resolve the infinitesimal vorticity layer at $t = 0^+$. To confine these errors to small times near $t = 0$, small initial time steps are used for all cases. For the first 20 time steps, $\Delta t = 10^{-4}$ is used. This is followed by 28 steps with $\Delta t = 10^{-3}$, which brings the time level to 0.03. A constant Δt (10^{-2} for $\alpha = 0.5$ and 1; 2.5×10^{-3} for $\alpha = 2.07$ and 3.25) is taken for the rest of each simulation. The time-step size is not dictated by the numerical stability constraint, but rather is chosen on the basis of accuracy considerations. To demonstrate the accuracy of the initial flow field, we show in figures 2(a-d) the variation of vorticity on the cylinder for four values of α at small times. The numerical results are compared to the asymptotic formula

$$\omega(1,\theta,t) \approx \frac{1}{\lambda}\left\{\alpha\left(2\pi^{-\frac{1}{2}} - \frac{\lambda}{2}\right) + \left(4\pi^{-\frac{1}{2}} + \lambda\right)\sin\theta + \left(2.7844\lambda - \frac{16}{3}\pi^{-\frac{3}{2}}\right)\alpha t\cos\theta\right\}$$
$$+ \frac{1}{\lambda}\left\{\left[6.5577\lambda - 4\pi^{-\frac{1}{2}}\left(1 + \frac{4}{3}\pi^{-1}\right)\right]t\sin 2\theta\right\}$$
(15)

given by Badr & Dennis (1985), where

$$\lambda = 2\left(\frac{2t}{Re}\right)^{\frac{1}{2}}.$$
(16)

We see that agreement with the asymptotic results improves as t increases. Better agreement is achieved for $\alpha = 2.07$ and 3.25 since a smaller time-step size is used. These results demonstrate that errors are indeed confined to a very limited time close to $t = 0$, as reported by Lugt & Haussling (1974).

5.1 $\alpha = 0.5$

In this subsection, we extend the computations of Badr & Dennis (1985) to larger dimensionless times than considered by them or in the experiments of Coutanceau & Ménard. The kinematics and dynamics of vortex shedding are discussed using instantaneous streamlines in two different reference frames, as well as vorticity distributions.

Figures 3(a-p) show a sequence of instantaneous streamlines for $1 \leq t \leq 24$, viewed from a nonrotating frame translating with the circular cylinder. The streamfunction is computed from the velocity field by a least-squares method described by Chen (1989). Comparison to the flow visualizations of Coutanceau & Ménard (1985) shown in figures 4(a,b) demonstrate the excellent agreement between our computations and their experiment. We see that the numerical results are virtually identical to the flow visualizations, as is also the case for the results of Badr & Dennis (1985). For $t \leq 13$, a detailed discussion of the flow development has been presented by Coutanceau & Ménard (1985), to which the reader is referred. We adopt their notation and observe that the coalescence of two "intermediate" eddies E_3' and E_3'' to form eddy E_3 at $t \approx$ 12 (figures 3i-j) indeed repeats [at $t \approx 22$; figures 3(n-o)] as predicted by Coutanceau & Ménard (1985). (The subscript here denotes the order of appearance of eddies after the impulsive start.) The transposition of saddle points S_2 and S_3' associated with eddies E_2 and E_3', respectively, discussed by Coutanceau & Ménard (1985) and sketched by Badr et al. (1986), is clearly shown in our figures 3(g-h). Also, a common boundary for E_2 and E_3', which was difficult to observe experimentally (Coutanceau & Ménard 1985) due to limitations of the flow visualization technique, does indeed exist, as shown in figure 3g. The common boundary soon becomes an "alleyway" for fluid to pass through, as shown in figure 3h. As noted by Eaton

(1987), existence of such an alleyway in an unsteady flow does not imply that fluid is carried from one side of the wake to the other.

As discussed by Perry et al. (1982), the streamlines are not invariant with respect to a change in reference frame, and the vortex street can appear very differently in different frames. To best observe the development of a vortex, the observer should move with its center (Lugt 1979). Otherwise, the vortex can be masked by the motion of the observer relative to the vortex (Williamson 1985; Coutanceau & Ménard 1985). This masking phenomenon was described by Coutanceau & Ménard as the opening up of vortices and disappearance of closure points into a wave-like pattern, as sketched in Lugt (1979). Since an _attached_ vortex translates with the cylinder, it can be clearly observed in a frame translating with the cylinder. However, after the vortex is shed into the fluid, its core is, especially in the far-wake, essentially stationary with respect to the undisturbed fluid, although it still moves slightly in the direction of the cylinder translation. Therefore, it is generally easier to observe _shed_ vortices in a frame fixed with the undisturbed fluid. The instantaneous streamlines observed in such a frame are shown at selected times in figures 5(a-c). As expected, the shed vortices are clearly distinguishable. We note that two additional vortices are shed over an interval of about 10 dimensionless time units, and that the vortex patterns near the cylinder are very similar in figures 5a and 5c. We further note that in a moving frame, the cylinder itself is not a streamline, and the attached vortices in figures 5(a-c) are now masked by the velocity field in the near wake of the cylinder. In a frame translating with the cylinder, however, the shed vortices are hidden in the oscillating wake, as shown in figures 6(a-c) for the values of t shown in figures 5(a-c). At the same dimensionless times, figures 7(a-c) show the corresponding vorticity contours, which are invariant with respect to translation of the observer. Because rotation divides the

surface of the cylinder into "downstream-moving" and "upstream-moving" parts, a basic symmetry of the vorticity field for the nonrotating ($\alpha = 0$) case [associated with the fact that for a T-periodic flow, the relations

$$u(r, \theta, t) = u(r, -\theta, t - \tau)$$
$$v(r, \theta, t) = -v(r, -\theta, t - \tau)$$

(17)

lead to $\omega(r, \theta, t) = -\omega(r, -\theta, t - \tau)$, where $0 < \tau < T$ is a phase difference] is broken. Nonetheless, the process is topologically similar to the $\alpha = 0$ case, with the shedding of vortices of alternating rotational sense being accompanied by thinning and severance of elongated vorticity contours emanating from opposite sides of the cylinder. As in the experiments of Díaz et al. (1983) at higher Re, cylinder rotation has the effect of altering the initial trajectories of the shed vortices, although these are expected to become parallel to the direction of cylinder translation as the vortices move farther away from the rotating cylinder and are advected downstream. As for $\alpha = 0$, vortices of opposite sense lie on opposite sides of a "street", although the rotation has clearly displaced the midline of the street upward.

Figures 8(a,b) show that the computation of vortex core and saddle locations using streamfunction values [in excellent agreement with those computed by Coutanceau & Ménard (1985)] can differ significantly from those computed using the vorticity distribution. For example, at $t = 7$, the streamwise location of the core of the first vortex is at about $x/a = 3.3$ as computed from the streamfunction data (in a frame translating with the cylinder), and a bit less than $x/a = 2.5$ as computed from the vorticity contours. This clearly illustrates the effect of streamline masking on vortices moving with velocities significantly different from the reference frame in which they are observed.

As a further check on the accuracy of our results, we show in figures 9(a,b) and 10(a,b) profiles of the velocity components at various locations. Also shown in these figures are representative data taken from the experiments of Coutanceau & Ménard (1985). Figures 9(a,b) show the temporal evolution of profiles of the u- and v-components of the velocity, respectively, along the x-axis in the wake of the cylinder for $t \leq 8$. Good quantitative agreement is obtained. In figures 10(a,b), we show the u-component above and below, respectively, the cylinder along the y-axis. Near the cylinder, agreement with experiment is very good. Farther from the cylinder, there is slightly more scatter in the experimental data. In this connection, we note that our results are graphically indistinguishable from those of Badr & Dennis (1985), although different numerical methods have been employed.

5.2 $\alpha = 1$

For $\alpha = 1$, figures 11(a-l) show instantaneous streamlines for $t \leq 24$, viewed from a nonrotating frame translating with the cylinder. These results are virtually identical to the flow visualizations [figures 9(a-h) of Coutanceau & Ménard (1985)]. Compared to the $\alpha = 0.5$ case, where the second eddy E_2 appears at $t \approx 2.0$, here E_2 and the third intermediate eddy E_3' are formed almost simultaneously at $t \approx 6.5$, as shown in figure 11c. During the next cycle of vortex formation, however, E_4 appears before E_5' is formed, as seen in figures 11(h,i). In general, the increase in α tends to inhibit the formation of the vortex at the downstream moving side of the cylinder, as reported in previous experiments (Díaz et al. 1983; Coutanceau & Ménard 1985).

Figures 12(a-e) show that the trajectories of the shed vortices for $\alpha = 1$ are qualitatively similar to those for $\alpha = 0.5$, except that the vortices shed from the downstream-moving side now lie above the midline of symmetry ($\theta = 0$), and due

to the counterclockwise fluid motion generated near the cylinder by its rotation, will remain above the midline during their subsequent advection downstream. Otherwise, the topology of the shedding process is altered relatively little, with vortices of alternating sense being shed from opposite sides of the cylinder, and subsequently being found on opposite sides of an albeit distorted "street" as they are advected downstream.

Figures 13(a,b) show the temporal evolution of profiles of the u-component and v-component, respectively, of the velocity along the x-axis in the wake of the cylinder for $t \leq 8$. Again, good agreement with experimental results (Coutanceau & Ménard 1985) is obtained.

5.3 $\alpha = 2.07$

As α increases, the vorticity layer generated at the upstream moving wall intensifies, resulting in even larger radial derivatives. Consequently, it becomes more difficult to maintain accuracy, as pointed out by Badr & Dennis (1985). We are able to achieve accurate numerical results by using finer radial grid spacings near the cylinder, as discussed in §3, and a smaller time-step size, as discussed at the beginning of this section. Figures 14(a-h) show instantaneous streamlines for $t \leq 24$, viewed from a nonrotating frame translating with the cylinder. For $t \leq 9$, our results are again virtually identical to the flow visualizations of Coutanceau & Ménard (1985), as shown in figures 15(a,b).

To better elucidate the vortex shedding process, we show in figures 16(a-f) the vorticity contours for $t \leq 24$. As for smaller values of α, vortex shedding still occurs for $\alpha = 2.07$, and consists of the shedding of vortices of alternating rotational sense from opposite sides of the cylinder. However, at this larger rotation rate the

asymmetry of the process is clear, and manifests itself in the considerably reduced strength of the vortices shed from the downstream-moving side of the cylinder [relative to those for $\alpha = 0.5$ shown in figures 7(a-c), and relative to those of opposite rotational sense for $\alpha = 2.07$], as well as in the fact that the shed vortices seem to be forming a "single file" line, rather than being paired off (according to rotational sense) on opposite sides of a "street". The relative weakness of the vortices shed from the downstream-moving side of the cylinder is due to the fact that immediately after the impulsive start, this part of the rotating boundary travels at about the same speed as the adjacent fluid. The weak vorticity layer generated near $\theta = 270°$ (shown in figure 2c) is responsible for the weakness of the shed vortex.

5.4 $\alpha = 3.25$

For $\alpha = 3.25$, figures 17(a-d) show instantaneous streamlines for $t \leq 24$, viewed from the reference frame given in figure 1. We note that our computational results at $t = 9$ differ slightly from the flow visualization of Coutanceau & Ménard (1985). We believe it is likely that this results from three-dimensional effects due to appreciable sidewall boundary layers for large values of α at large time in the experiments, as discussed by Coutanceau & Ménard (1985). We note that although for $\alpha = 0$, the nominally two-dimensional flow at $Re = 200$ is unstable with respect to three-dimensional disturbances (Williamson 1988), no information regarding the effect of rotation on the stability appears to be available. Computed vorticity contours are shown for $t \leq 54$ in figures 18(a-h). At $t = 24$, figure 18c shows that the elongated vorticity contour has not yet been severed. To investigate whether the vortex shedding process continues to larger t for this value of α, we let the size of the computational domain grow linearly in time until $t = 54$ in order to extend the computation. The

same values of s_0 and s_1 in the stretching function are used to distribute 120 circular grid lines between $r = 1$ and $r = 1.5t - 12$. The numerical solution at $t = 54$ is not very accurate since the vorticity at the outer perimeter ($r = 69$) is not negligible (on the order of 10^{-1} or smaller) at the end of the simulation. Nonetheless, we believe that our computation of the vortex shedding in the near wake is qualitatively correct, even for $t > 32$ (at which time the maximum of the absolute value of the vorticity on the outer boundary is less than 4×10^{-4}). Figure 18e shows that the second vortex is shed into the fluid as for smaller α, although shedding here occurs at a much later time. However, even in a reference frame fixed with the undisturbed fluid, the weak second vortex is masked by the high velocity induced in the near wake by the rapidly rotating cylinder. Therefore, for large α it is not surprising that previous flow visualization experiments, including those performed in a frame translating with the cylinder, have failed to reveal the shedding of a second (weaker) vortex. Moreover, in the transient experiments of Coutanceau & Ménard (1985), experimental limitations prevented continuation of the flow to the dimensionless time at which the second vortex would have been shed. These difficulties have led to the erroneous conclusions that for $\alpha > 2.5$ (or $\alpha > 1$), no vortices are shed after the initial (strong) starting vortex, and that the vortex street is completely destroyed.

To render the second vortex distinguishable, we show in figure 19a the streamlines at $t = 32$ in a reference frame moving with the core of the second vortex. Experimentally, this would be a difficult task since a camera would have to move with the vortex core velocity vector (u_c, v_c) relative to the cylinder, which is not known *a priori*. Numerically, this is achieved by simply subtracting streamfunction values corresponding to the velocity (u_c, v_c) of the vortex core from those in the reference frame fixed with the cylinder. The second vortex is clearly visible in a frame moving

with the core of the third vortex (figure 19b), while the first vortex is still sufficiently strong to be visible in this reference frame (in which its core velocity is nonzero).

5.5 Temporal evolution of the lift and drag coefficients

Finally, we present the temporal evolution of the lift and drag coefficients defined by

$$C_L = \frac{L}{\rho U^2 a} \tag{18}$$

and

$$C_D = \frac{D}{\rho U^2 a} \tag{19}$$

where L and D are the lift and drag forces acting on the cylinder, respectively, and ρ is the density of the fluid. Integrating the pressure and shear stresses over the surface of the cylinder, we can express these in r-θ coordinates as

$$C_L = C_{Lp} + C_{Lf} = \frac{2}{Re} \int_0^{2\pi} \left[-\left(\frac{\partial \omega}{\partial r}\right)_b + \omega_b \right] \cos \theta \, d\theta \tag{20}$$

and

$$C_D = C_{Dp} + C_{Df} = \frac{2}{Re} \int_0^{2\pi} \left[\left(\frac{\partial \omega}{\partial r}\right)_b - \omega_b \right] \sin \theta \, d\theta, \tag{21}$$

where the subscripts p and f denote contributions due to the pressure and friction, respectively, and the subscript b denotes quantities evaluated on the cylinder. We note that (20) and (21) differ from the expressions given by Badr et al. (1989) by a sign, due to a difference in the definition of vorticity. Figures 20(a,b) show the temporal evolution of the lift and drag coefficients at various α for $t \leq 24$. The

23

negative values of C_L indicate that the lift force is in the $-y$ direction. The time-periodic nature of C_L is well established for $\alpha = 0.5$ and 1. At higher values of α, however, a longer time-span is required for periodicity to be established since the second and subsequent eddies form and are shed much later, as discussed above. In figures 21(a,b), the pressure and skin friction contributions to the lift and drag are drawn separately for $\alpha = 1$. Similarly small viscous contributions to C_L and C_D are found for all other values of α investigated. It is clear that lift and drag are largely due to the pressure force, consistent with previous work showing that the Magnus effect is primarily an inviscid phenomenon.

6. Conclusion

Our computations of the temporal development of the flow generated by a circular cylinder started impulsively from rest into steady rotatory and rectilinear motion at $Re = 200$ show that for the largest value of α (3.25) investigated by Coutanceau & Ménard (1985), vortex shedding continues after the first vortex is shed, contrary to earlier conclusions. That these authors were led to conclude that sufficiently high values of α suppress vortex shedding at $Re = 200$ is likely due to the fact that their experimental facility did not allow for visualization of the flow for a long enough time. Even if that limitation had been overcome, however, it is likely that their flow visualization technique (which approximately yields instantaneous streamlines) would have failed to reveal the presence of the second vortex, due to masking by the large velocities induced in the near wake by the rapidly rotating cylinder.

We note that for $\alpha = 3.25$ the time interval between the shedding of the first and second vortices is much longer than the time required to shed the first. We conjecture that for subsequent vortices, the interval between shedding of the 2n-th and (2n+1)-

24

th vortices will be considerably shorter than the interval between shedding of the (2n+1)-th and (2n+2)-th.

We also observe that for α = 2.07 and 3.25, the second vortex (shed from the downstream-moving side of the cylinder) is much smaller than the first, and conjecture that, in general, the 2n-th vortex shed will be significantly smaller than the (2n+1)-th. Unlike the nonrotating (α = 0) case, there is no requirement that the vortices shed from opposite sides of the cylinder be of equal magnitude, or even that consecutive vortices must be shed alternately from opposite sides of the cylinder. In fact, there does not appear to be any reason why vortices cannot be shed from a single (upstream moving) side of the cylinder. Thus, we further conjecture that for a given Re, there exists a critical value of α beyond which vortex shedding occurs from only one side of the cylinder.

From the standpoint of controlling laminar two-dimensional vortex shedding from a circular cylinder by using either "active" control [a term that in the fluid mechanics literature has come to mean a time-periodic, and frequently harmonic input, e.g., $\Omega(t + T) = \Omega(t)$ or $\Omega(t) = \Omega_0 \sin 2\pi f t$] or feedback control, the present calculations show that the nature of the vorticity field as well as the vortex shedding process can be significantly altered by cylinder rotation. To the best of our knowledge, the only investigations to date concerning the effect of a time-dependent rotation rate on the shedding process are the experimental studies of Taneda (1977, 1978) and Tokumaru & Dimotakis (1989), and the combined experimental and theoretical studies by Okajima, Takata & Asanuma (1975), Mo (1989), and Wu, Mo & Vakili (1989).

The experimental work of Taneda (1978) for 30 $\leq$ Re $\leq$ 300 [including the range in which Hopf bifurcation (Jackson 1987, Zebib 1987) of the steady two-dimensional flow at Re $\approx$ 45 leads to unsteady asymmetric two-dimensional solutions

exhibiting vortex shedding] shows that for sufficiently large values of the amplitude and frequency of time-harmonic rotatory oscillations, vortex shedding (and indeed the formation of attached vortices) can be eliminated. Moreover, Taneda's flow visualizations (see his figure 3d) indicate that under certain circumstances, a flow can be generated which is symmetric about $\theta = 0$ at at least one phase during the forcing cycle. This suggests that the flow can be driven to a symmetric state, and provides reason to believe that it can be stabilized (in the control-theoretic sense; cf. Kuo 1975) about a symmetric state in which no vortex shedding occurs.

Acknowledgments

REFERENCES

Badr, H. M., Dennis, S. C. R. & Young, P. J. S. 1989 Steady and unsteady flow past a rotating circular cylinder at low Reynolds numbers. *Computers & Fluids* **17**, 579-609.

Badr, H., Coutanceau, M., Dennis, S. & Ménard, C. 1986 On the phenomenon of vortex transposition and coalescence in separated flows. *Comptes Rend. Acad. Sci.* **302 II**, 1127-1130.

Badr, H. M. & Dennis, S. C. R. 1985 Time-dependent viscous flow past an impulsively started rotating and translating circular cylinder. *J. Fluid Mech.* **158**, 447-488.

Chen, Y.-M. 1989 Numerical simulation of the unsteady two-dimensional flow in a time-dependent doubly-connected domain. Ph.D. dissertation, University of Arizona.

Chen, Y.-M., Koniges, A. E. & Anderson, D. V. 1989 ILUBCG2-11: Solution of 11-banded nonsymmetric linear equation systems by a preconditioned biconjugate gradient routine. *Comp. Phys. Comm.* **55**, 359-365.

Chen, Y.-M. & Pearlstein, A. J. 1991 General numerical procedure for determination of the boundary vorticity in velocity/vorticity formulations of the Navier-Stokes equations. To be submitted to *J. Comp. Phys.*

Collins, W. M. & Dennis, S. C. R. 1973 Flow past an impulsively started circular cylinder. *J. Fluid Mech.* **60**, 105-127.

Coutanceau, M. & Ménard, C. 1985 Influence of rotation on the near-wake development behind an impulsively started circular cylinder. *J. Fluid Mech.* **158**, 399-446.

Díaz, F., Gavaldá, J., Kawall, J. G., Keffer, J. F. & Giralt, F. 1983 Vortex shedding from a spinning cylinder. *Phys. Fluids* **26**, 3454-3460.

Eaton, B. E. 1987 Analysis of laminar vortex shedding behind a circular cylinder by computer-aided flow visualization. *J. Fluid Mech.* **180**, 117-145.

Fasel, H. 1976 Investigation of the stability of boundary layers by a finite-difference model of the Navier-Stokes equations *J. Fluid Mech.* **78**, 355-383.

Fornberg, B. 1980 A numerical study of steady viscous flow past a circular cylinder. *J. Fluid Mech.* **98**, 819-855.

Glauert, M. B. 1957a A boundary layer theorem, with applications to rotating cylinders. *J. Fluid Mech.* **2**, 89-99.

Glauert, M. B. 1957b The flow past a rapidly rotating circular cylinder. *Proc. Roy. Soc. Lond.* A **242**, 108-115.

Ingham, D. B. 1983 Steady flow past a rotating cylinder. *Computers & Fluids* **11**, 351–366.

Ingham, D. B. & Tang, T. 1990 A numerical investigation into the steady flow past a rotating circular cylinder at low and intermediate Reynolds numbers. *J. Comp. Phys.* **87**, 91-107.

Jackson, C. P. 1987 A finite-element study of the onset of vortex shedding in flow past variously shaped bodies. *J. Fluid Mech.* **182**, 23-45.

Koromilas, C. A. & Telionis D. P. 1980 Unsteady laminar separation: an experimental study. *J. Fluid Mech.* **97**, 347-384.

Kuo, B. 1975 *Automatic Control Systems*, 3rd Edition, Prentice-Hall, Englewood Cliffs.

Lugt, H. J. 1979 The dilemma of defining a vortex. In *Recent Developments in Theoretical and Experimental Fluid Mechanics*, U. Müller, K. G. Roesner, and B. Schmidt, Eds., pp. 309-321, Springer-Verlag.

Lugt, H. J. & Haussling, H. J. 1974 Laminar flow past an abruptly accelerated elliptic cylinder at 45° incidence. *J. Fluid Mech.* **65**, 711-734.

Lyulka, V. A. 1977 Numerical solution of the problem of the rotation of a cylinder in a flow of a viscous incompressible fluid. *Zh. Vychisl. Mat. mat. Fiz.* **17**, 470-480. (Translated in *USSR Computational Mathematics and Mathematical Physics* **17** (2) 178-188, 1978.)

Mo, J. 1989 An investigation of wake flow around a cylinder with rotational oscillations. Ph.D. dissertation, University of Tennessee Space Institute.

Modi, V. J., Mokhtarian, F. & Yokomizo, T. 1990 Effect of moving surfaces on the airfoil boundary-layer control. *J. Aircraft* **27**, 42-50.

Moore, D. W. 1957 The flow past a rapidly rotating cylinder in a uniform stream. *J. Fluid Mech.* **2**, 541-550.

Okajima, A., Takata, H. & Asanuma, T. 1975 Viscous flow around a rotationally oscillating circular cylinder. Report No. 532, Institute of Space and Aeronautical Science, University of Tokyo.

Orszag, S. A. 1980 Spectral methods for problems in complex geometries. *J. Comp. Phys.* **37**, 70-92.

Perry, A. E., Chong, M. S. & Lim, T. T. 1982 The vortex-shedding process behind two-dimensional bluff bodies. *J. Fluid Mech.* **116**, 77-90.

Prandtl, L. 1925 The Magnus effect and windpowered ships. *Naturwissenschaften* **13**, 93-108.

Prandtl, L. & Tietjens, O. G. 1934 *Applied Hydro- and Aeromechanics* (transl. J. P. Den Hartog 1957). Dover.

Reddy, R. N. & Thompson, J. F. 1977 Numerical solution of incompressible Navier-Stokes equations in the integro-differential formulation using boundary-fitted coordinate systems. AIAA Paper 77-650.

Shkadova, V. P. 1982 Rotating cylinder in a flowing viscous incompressible fluid. *Akad. Nauk SSSR, Izv. Mekh. Zhidk. Gaza* (1) 16-21. (Translated in *Fluid Dynamics* **17**, (1) 12-16, 1982.)

Simuni, L. M. 1967 Solution of certain problems in flow of a viscous fluid, associated with a cylinder and a sphere. *Izv. Sib. Otdel. Akad. Nauk SSSR, Ser. Tekh. Nauk* (2) 23-28.

Swanson, W. M. 1961 The Magnus effect: a summary of investigations to date. *ASME J. Basic Engrg.* **83**, 461-470.

Ta Phuoc Loc 1975 Étude numérique de l'écoulement d'un fluide visqueux incompressible autour d'un cylindre fixe ou en rotation. Effet Magnus. *J. Méc.* **14**, 109-134.

Taneda, S. 1977 Visual study of unsteady separated flows around bodies. *Prog. Aero. Sci.* **17**, 287-348.

Taneda, S. 1978 Visual observations of the flow past a circular cylinder performing a rotatory oscillation. *J. Phys. Soc. Japan* **45**, 1038-1043.

Taneda, S. 1980 Visualization of unsteady flow separation. In *Flow Visualization* II, ed. W. Merzkirch, pp. 253-257, Hemisphere.

Taslim, M. E., Kinney, R. B. & Paolino, M. A. 1984 Analysis of two-dimensional viscous flow over cylinders in unsteady motion. *AIAA J.* **22**, 586-594.

Telionis, D. P. 1981 *Unsteady Viscous Flows*. Springer-Verlag.

Tennant, J. S., Johnson, W. S. & Krothapalli, A. 1976 Rotating cylinder for circulation control on an airfoil. *J. Hydronautics* **10**, 102-105.

Ting, L. 1983 On the application of the integral invariants and decay laws of vorticity distributions. *J. Fluid Mech.* **127**, 497-506.

Tokumaru, P. T. & Dimotakis, P. E. 1989 Rotary oscillation control of a cylinder wake. AIAA paper 89-1023, presented at AIAA 2nd Shear Flow Conference, Tempe, Ariz., March 13-16, 1989.

Townsend, P. 1980 A numerical simulation of Newtonian and visco-elastic flow past stationary and rotating cylinders. *J. Non-Newtonian Fluid Mech.* **6**, 219-243.

Vinokur, M. 1983 On one-dimensional stretching functions for finite-difference calculations. *J. Comp. Phys.* **50**, 215-234.

Wambecq, A. 1978 Rational Runge-Kutta methods for solving systems of ordinary differential equations. *Computing* **20**, 333-342.

Wang, C. M. & Wu, J. C. 1986 Numerical solution of steady Navier-Stokes problems using integral representations. *AIAA J.* **24**, 1305-1312.

Werlé, H. 1984 Hydrodynamic visualization of the flow around a streamlined cylinder with suction. Cousteau-Malavard turbine sail model. *La Recherche Aérospatiale* (English Edition), 4, 29-38.

Weston, R. P. & Liu, C. H. 1982 Approximate boundary condition procedure for the two-dimensional numerical solution of vortex wakes. AIAA paper 82-0951.

Williamson, C. H. K. 1985 Sinusoidal flow relative to circular cylinders. *J. Fluid Mech.* **155**, 141-174.

Williamson, C. H. K. 1988 The existence of two stages in the transition to three-dimensionality on a cylinder wake. *Phys. Fluids* **31**, 3165–3168.

Wood, W. W. 1957 Boundary layers whose streamlines are closed. *J. Fluid Mech.* **2**, 77-87.

Wu, J., Mo, J. & Vakili, A. 1989 On the wake of a cylinder with rotational oscillations. AIAA paper 89-1024, presented at AIAA 2nd Shear Flow Conference, Tempe, Ariz., March 13-16, 1989.

Wu, J. C. 1975 Velocity and extraneous boundary conditions of viscous flow problems. AIAA paper 75-47.

Wu, J. C. 1976 Numerical boundary conditions for viscous flow problems. *AIAA J.* **14**, 1042-1049.

Wu, J. C. & Sampath, S. 1976 A numerical study of viscous flow around an airfoil. AIAA Paper 76-337.

Wu, J. C. & Thompson, J. F. 1973 Numerical solutions of time-dependent incompressible Navier-Stokes equations using an integro-differential formulation. *Computers & Fluids* **1**, 197-215.

Zang, T. A., Wong, Y. S. & Hussaini, M. Y. 1982 Spectral multigrid methods for elliptic equations. *J. Comp. Phys.* **48**, 485-501.

Zebib, A. 1987 Stability of viscous flow past a circular cylinder. *J. Engrg. Math.* **21**, 155-165.
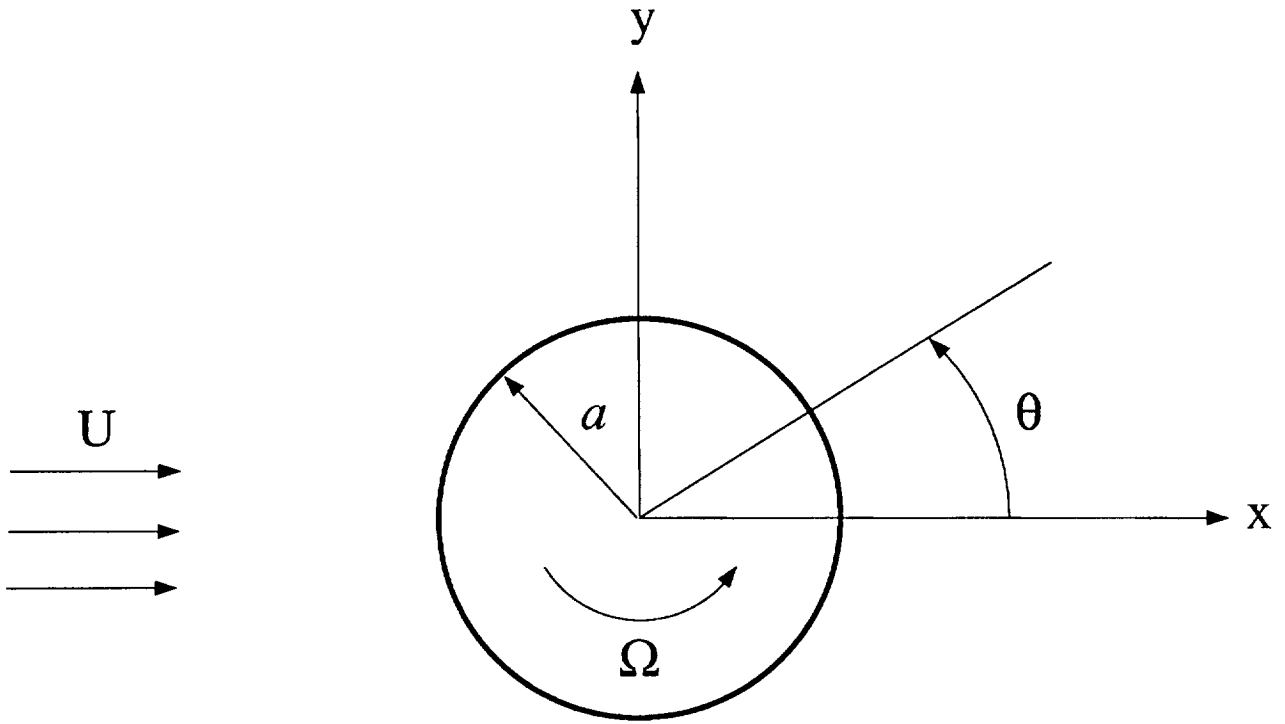
FIGURE 1. The reference frame.
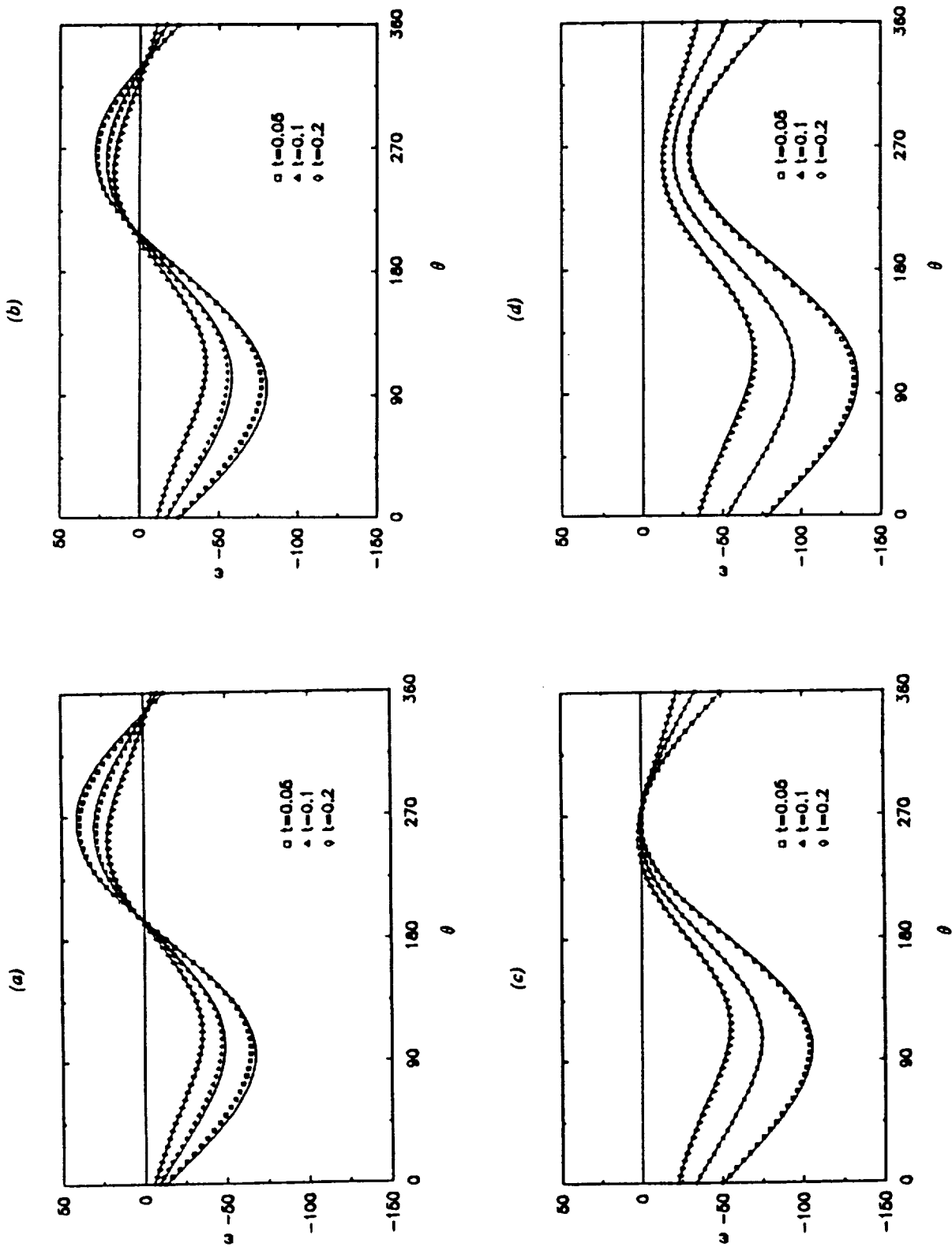
FIGURE 2. Evolution of the vorticity distribution on the surface of the cylinder at early times, $Re = 200$. ————: numerical solution; symbols: asymptotic solution. □, $t = 0.05$; △, $t = 0.1$; ◇, $t = 0.2$. (a) $\alpha = 0.5$, (b) $\alpha = 1.0$, (c) $\alpha = 2.07$, (d) $\alpha = 3.25$.

34

(a)

(b)

(c)

(d)
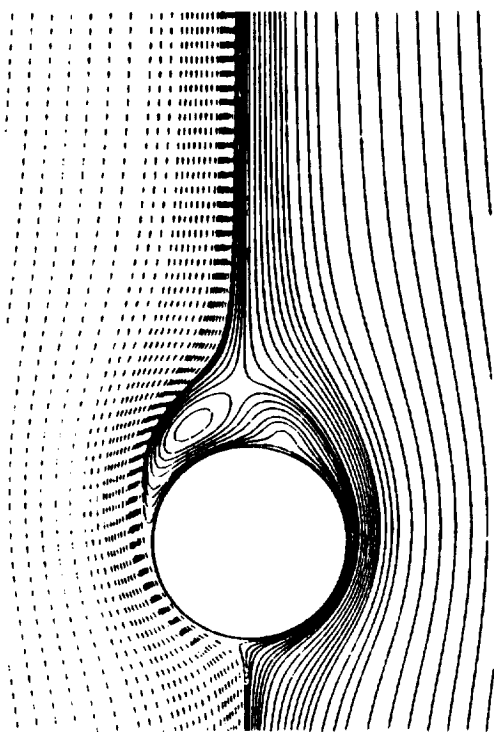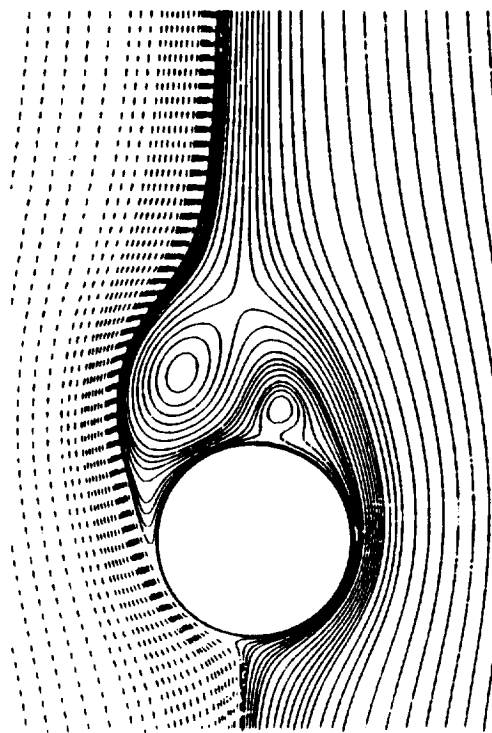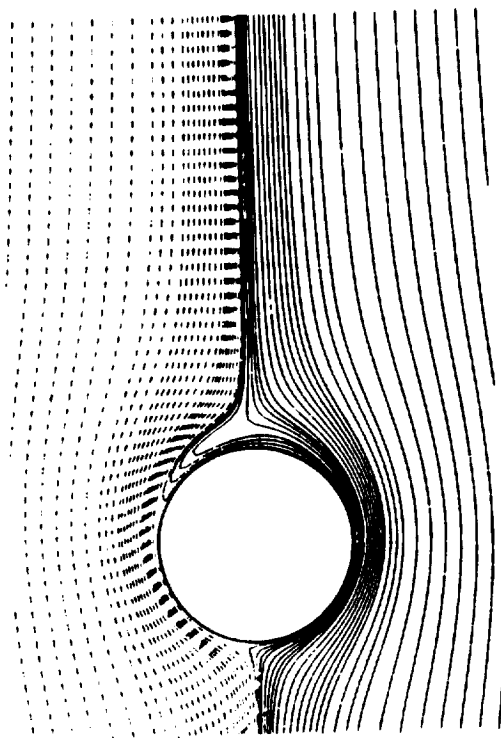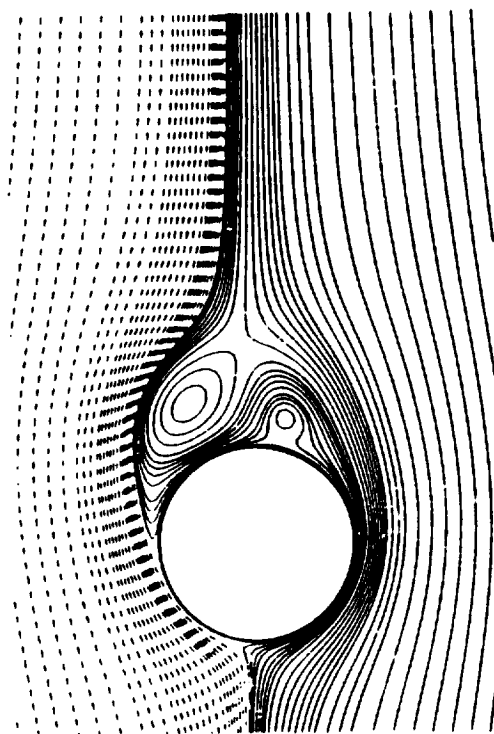
FIGURE 3 (a-d). For caption see page 38

35

(e)

(f)

(g)

(h)
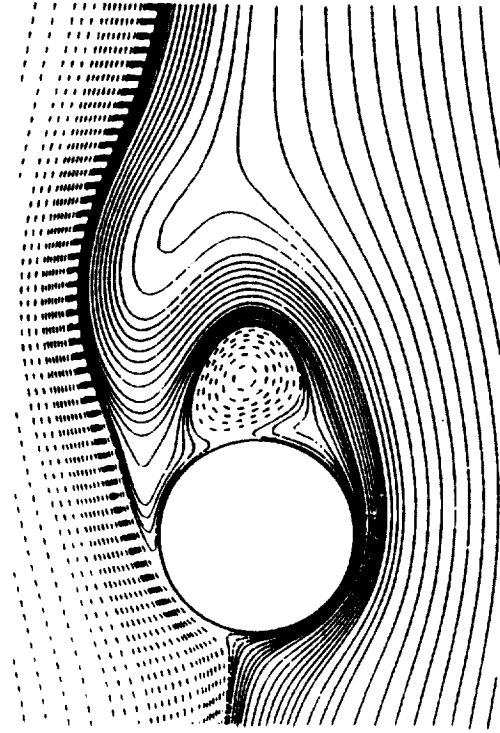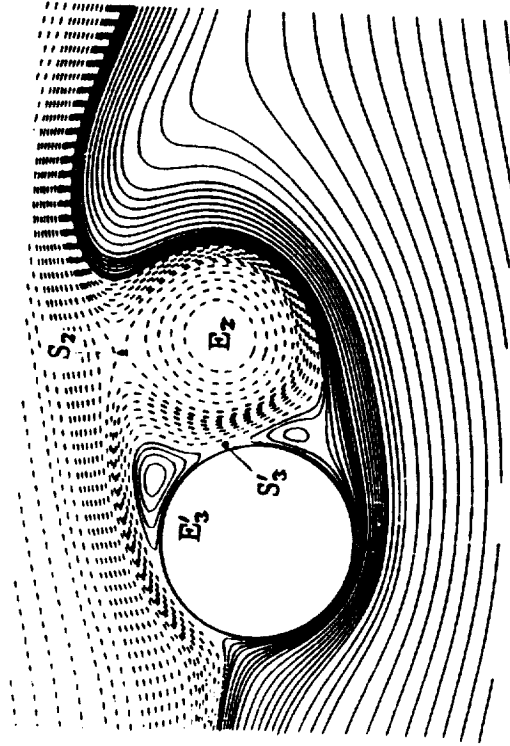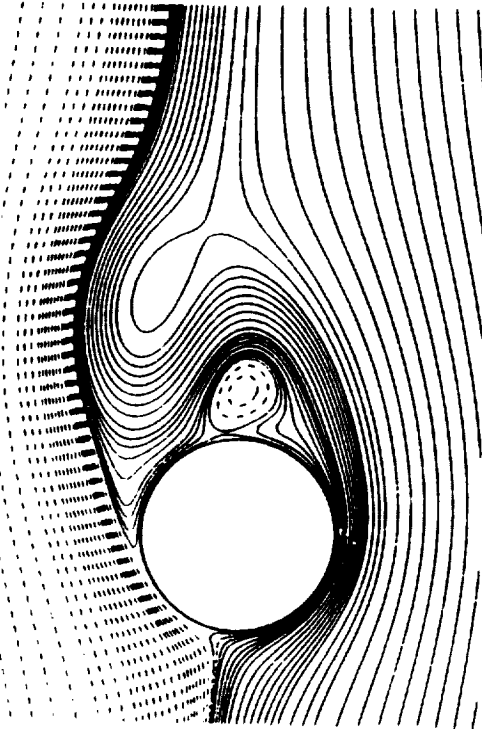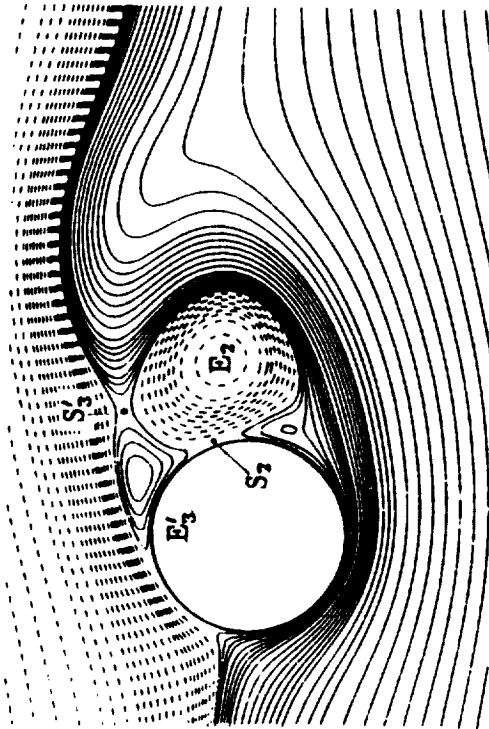
FIGURE 3 (e-h). For caption see page 38

36

(j)

(l)

(i)

E_3'

E_3''

E_3
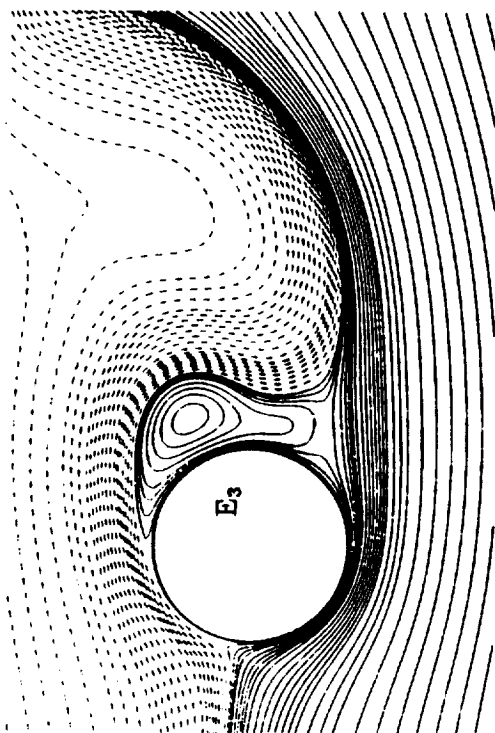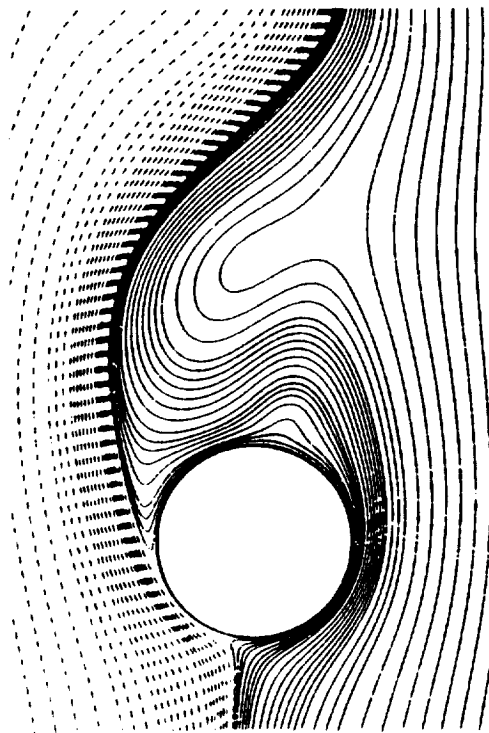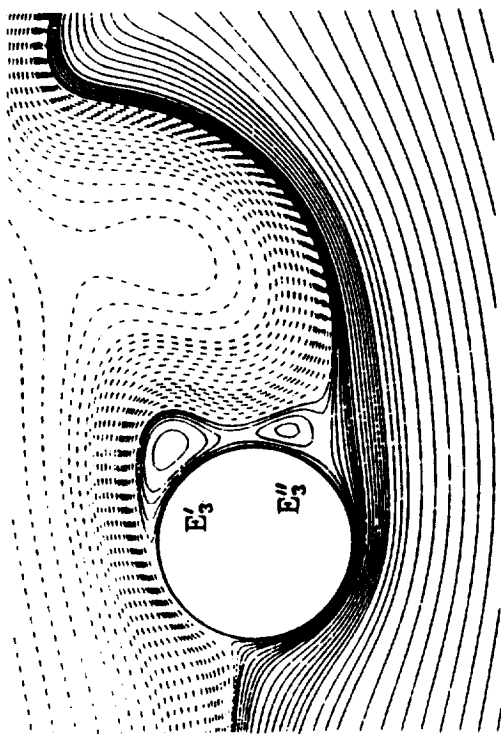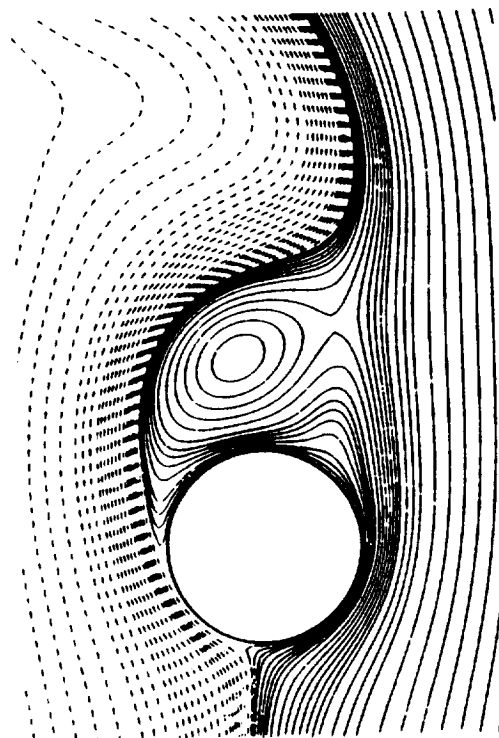
(k)

FIGURE 3 (i-l). For caption see page 38

37

(m)

(n)

(o)

(p)
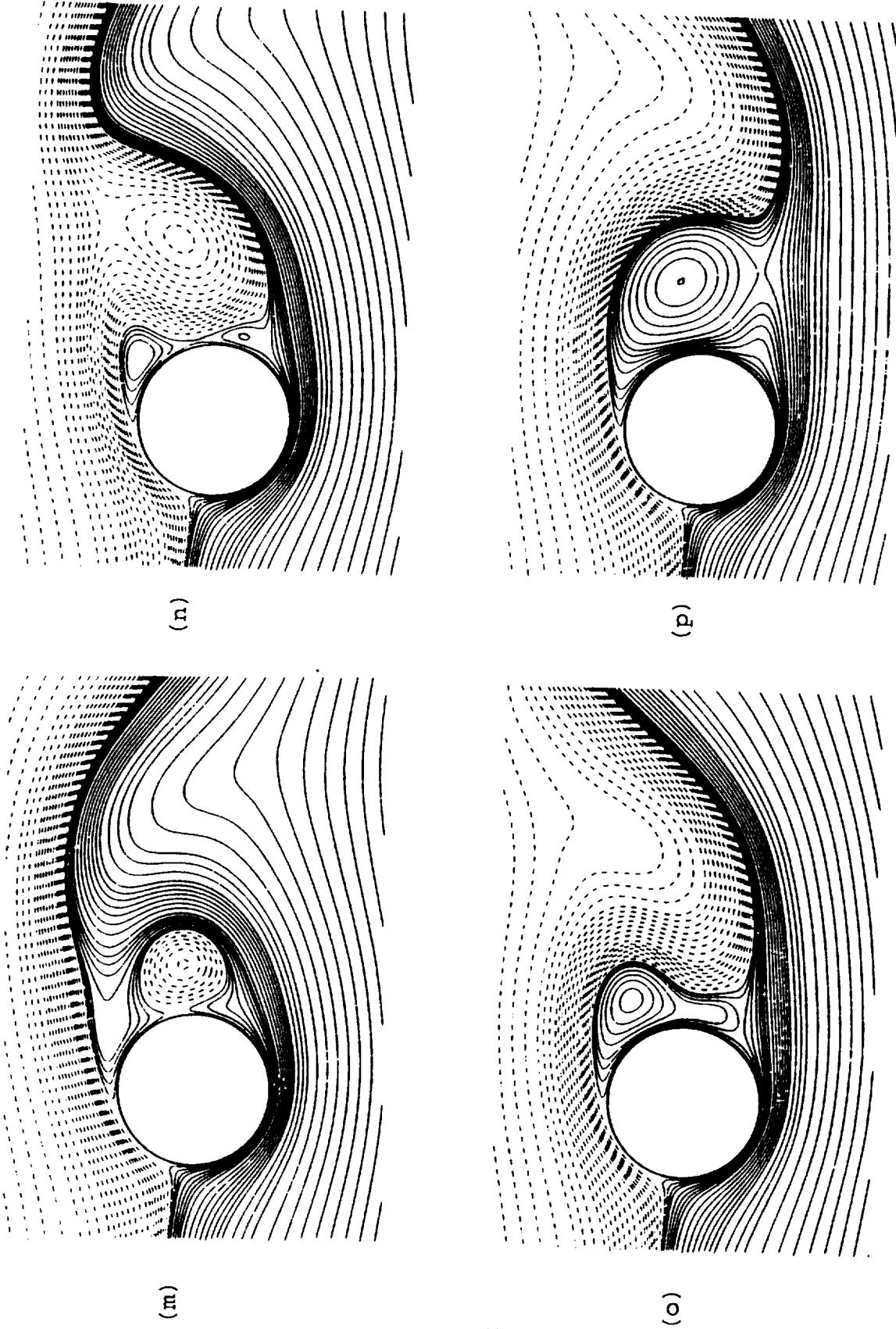
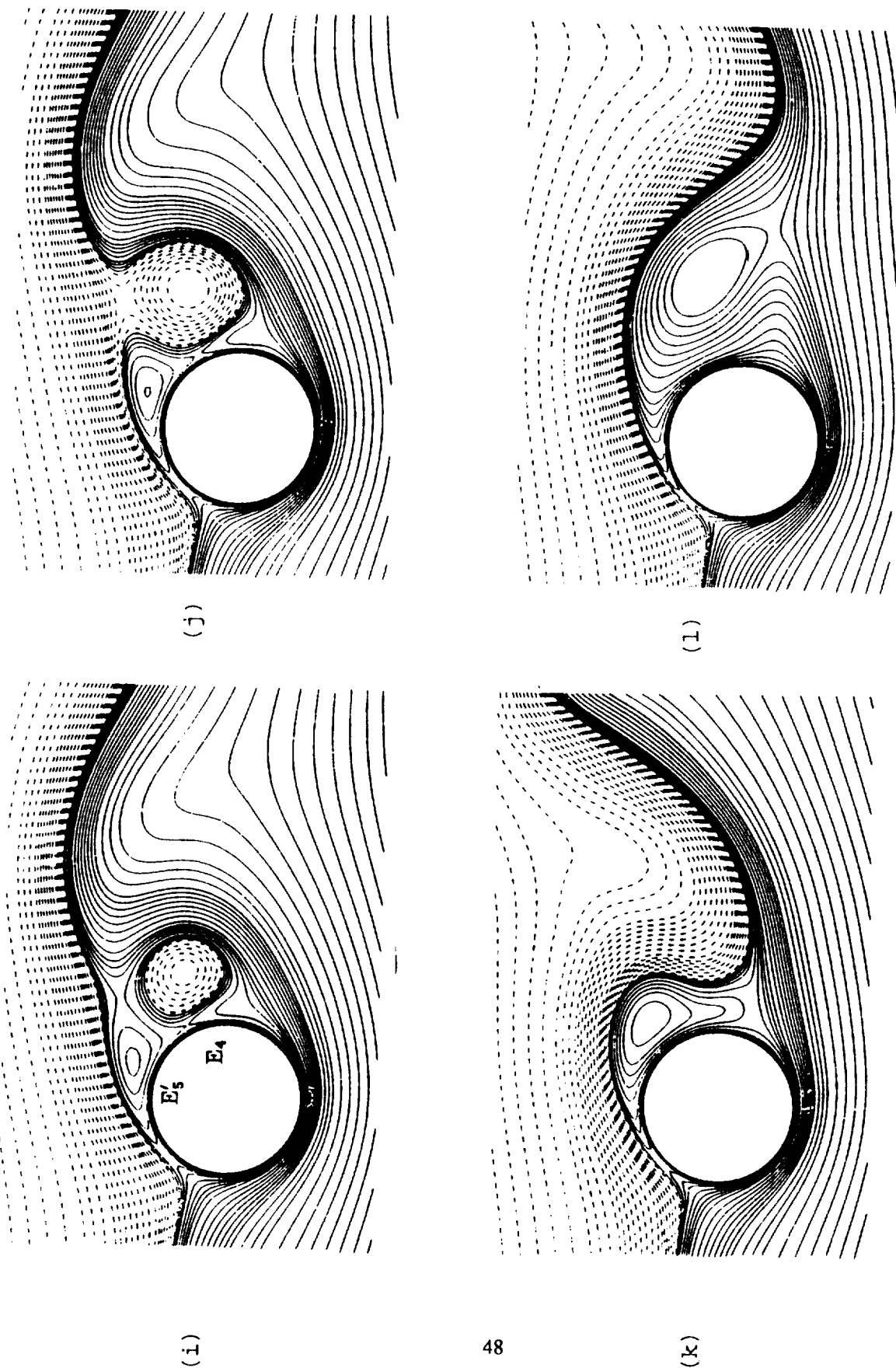**FIGURE 3.** Instantaneous streamlines for $Re = 200$, $\alpha = 0.5$ at various times, viewed from the reference frame in figure 1. Streamlines with positive (including zero) and negative streamfunction values (ψ) are shown by dashed and solid lines, respectively. In each diagram, the cylinder is a streamline with $\psi = 0$. The values of ψ plotted are 0.0, -0.01, ±0.02, -0.03, ±0.04, ±0.06, ±0.08, ±0.10, ±0.12, ±0.15, ±0.20, ±0.25, ±0.30, ±0.35, ±0.40, ±0.45, ±0.50, ±0.60, ±0.70, ±0.80, ±1.00 and an increment of ±0.2 thereafter. (a) $t = 1.0$, (b) $t = 2.0$, (c) $t = 3.0$, (d) $t = 4.0$, (e) $t = 6.0$, (f) $t = 7.0$,(g) $t = 8.0$, (h) $t = 9.0$,(i) $t = 11.0$, (j) $t = 12.0$, (k) $t = 14.0$, (l) $t = 16.0$, (m) $t = 18.0$, (n) $t = 20.0$, (o) $t = 22.0$, (p) $t = 24.0$.

38
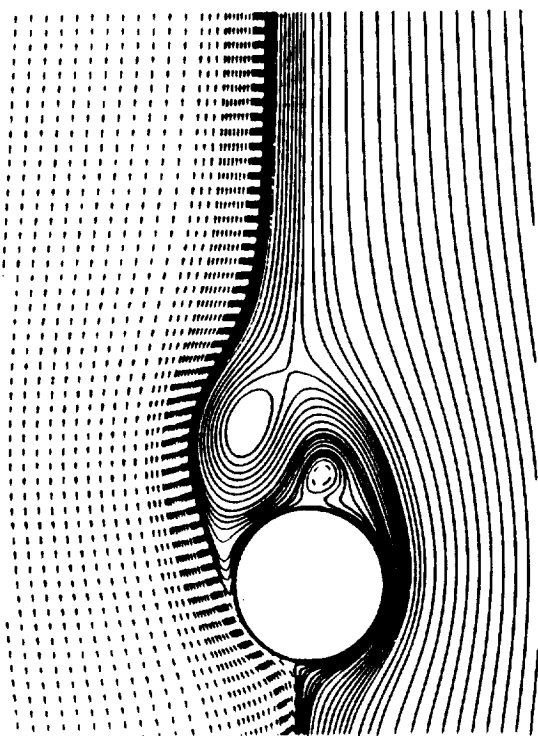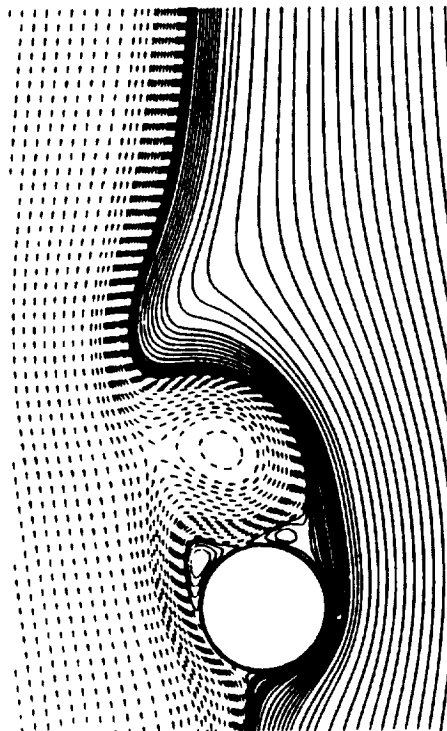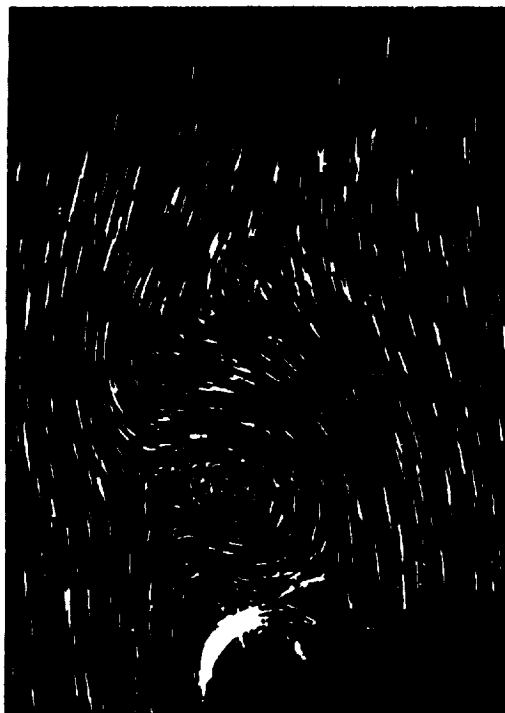
FIGURE 4. Comparison of calculated (left) and experimental (right) instantaneous streamlines for $Re = 200$, $\alpha = 0.5$. (a) $t = 5.0$, (b) $t = 10.0$.

(a)

(b)
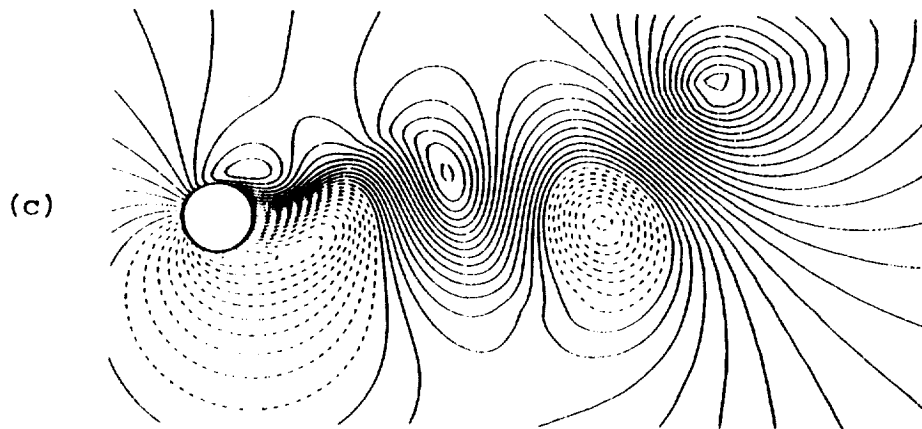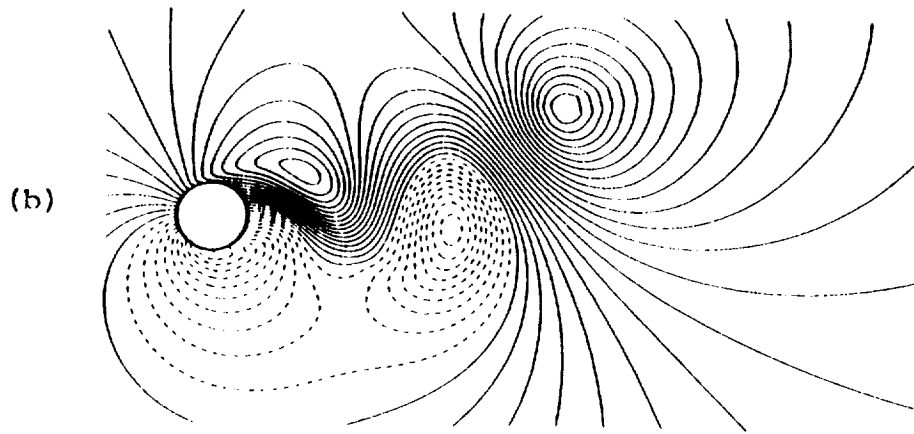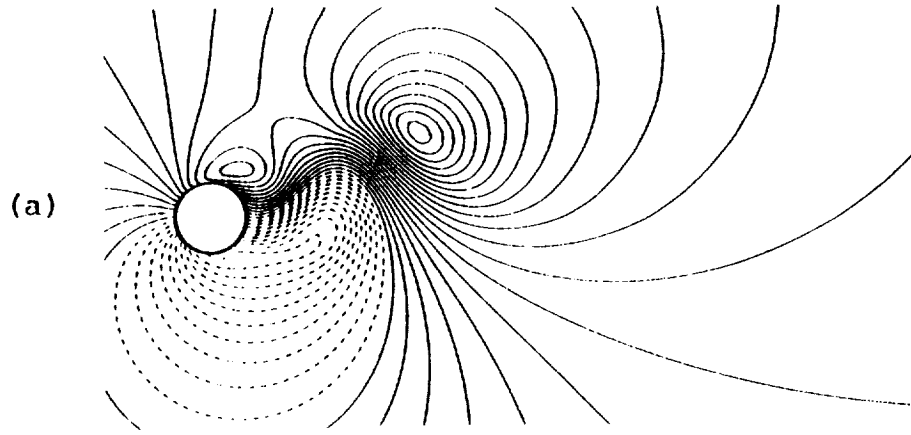
FIGURE 5. Instantaneous streamlines for $Re = 200$, $\alpha = 0.5$, viewed from a frame fixed with the undisturbed fluid. Dashed (solid) lines represent constant positive (negative) streamfunction values with $\Delta\psi = 0.1$ between them. (a) $t = 12.0$, (b) $t = 17.0$, (c) $t = 22.0$.
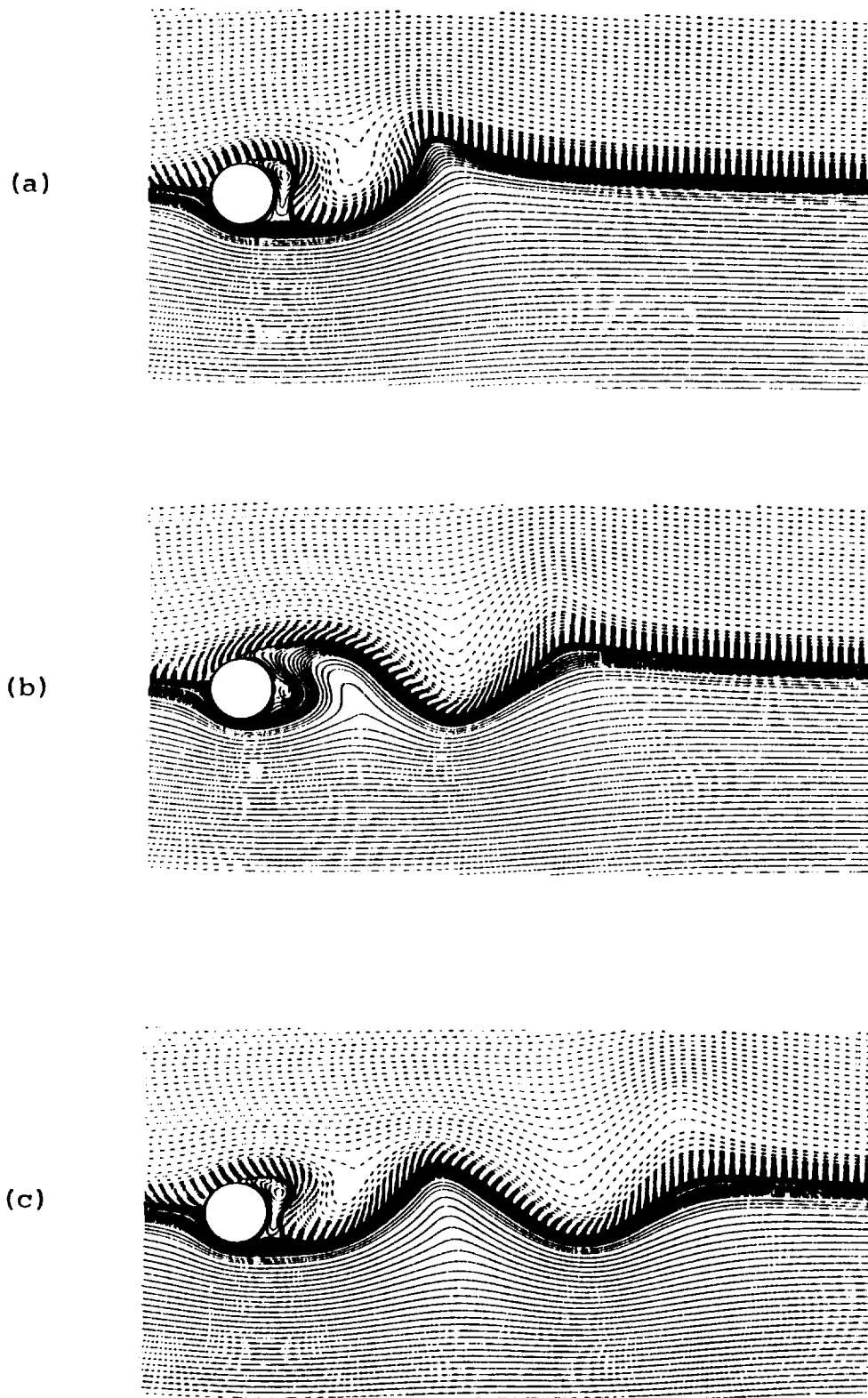
FIGURE 6. Instantaneous streamlines for $Re = 200$, $\alpha = 0.5$, viewed from the reference frame in figure 1. The plotting convention and contour levels as in figure 3. (a) $t = 12.0$, (b) $t = 17.0$, (c) $t = 22.0$.
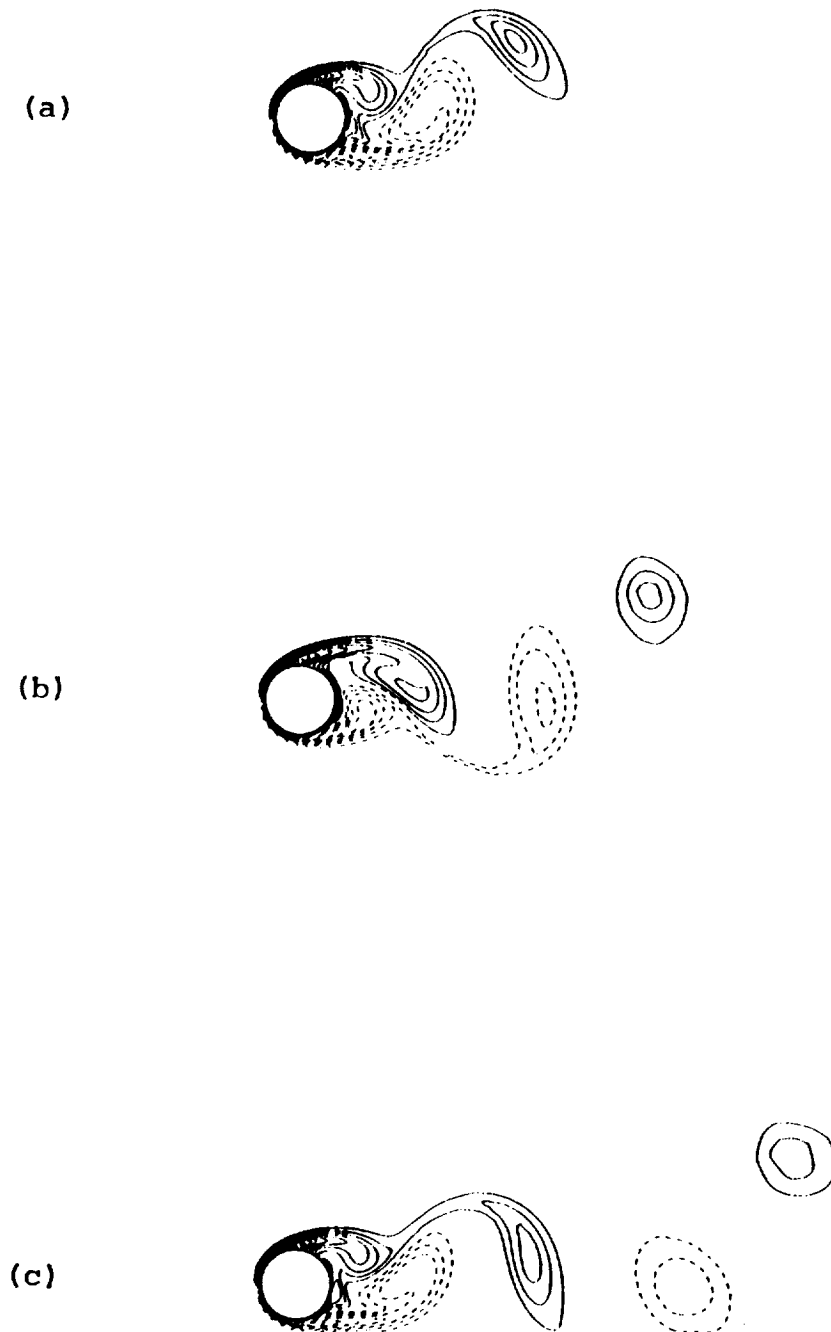
FIGURE 7. Equi-vorticity contours for $Re = 200$, $\alpha = 0.5$. Dashed (solid) lines represent constant positive (negative) vorticity values with a constant increment of 0.5. Vorticity contours with magnitude less than 0.5 are omitted for graphical clarity. (a) $t = 12.0$, (b) $t = 17.0$, (c) $t = 22.0$.
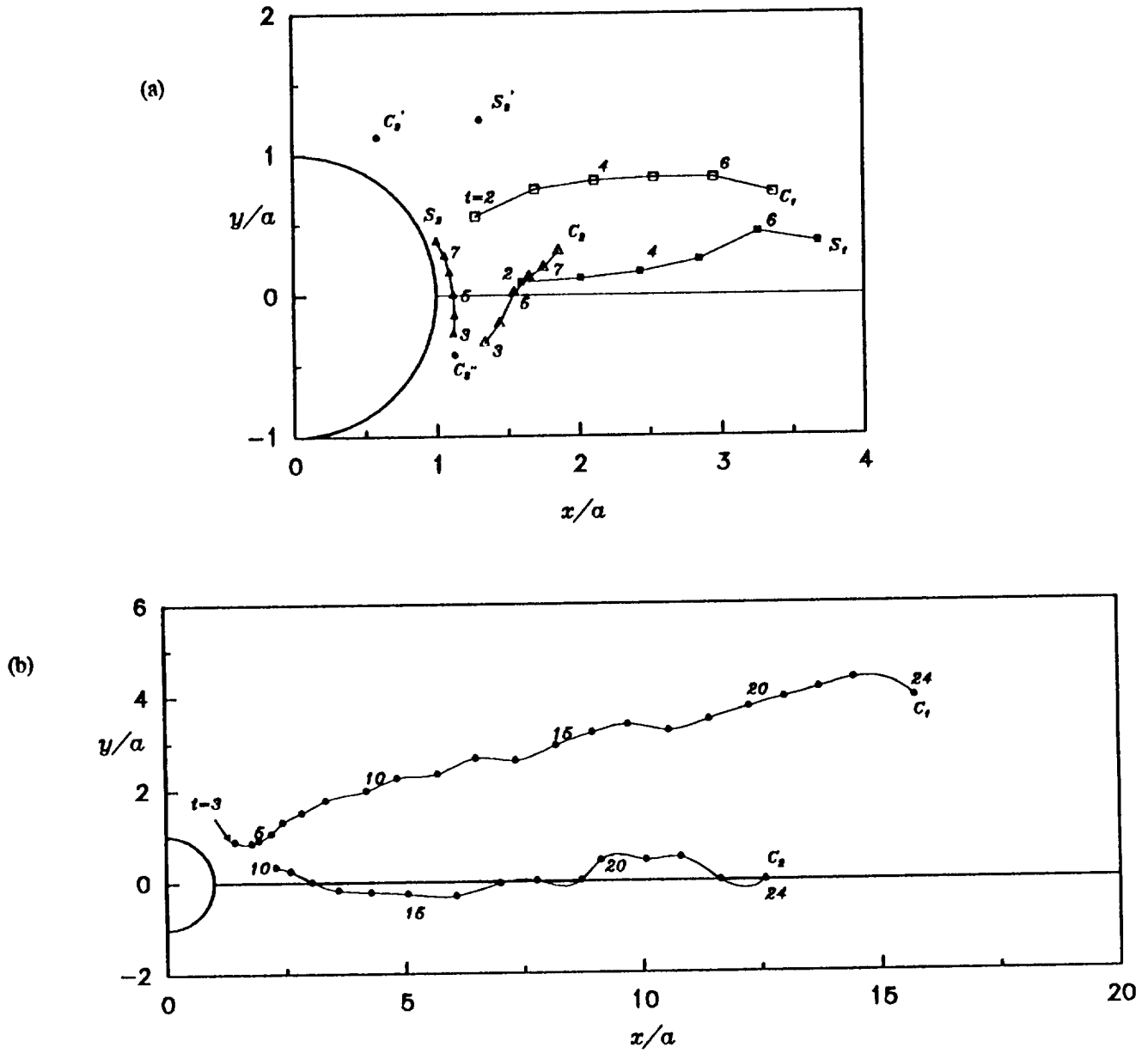
FIGURE 8. Trajectories of the centers C_i and the closure points S_i obtained from (a) Instantaneous streamline plots (b) equi-vorticity contours plots for $Re = 200$, $\alpha = 0.5$.
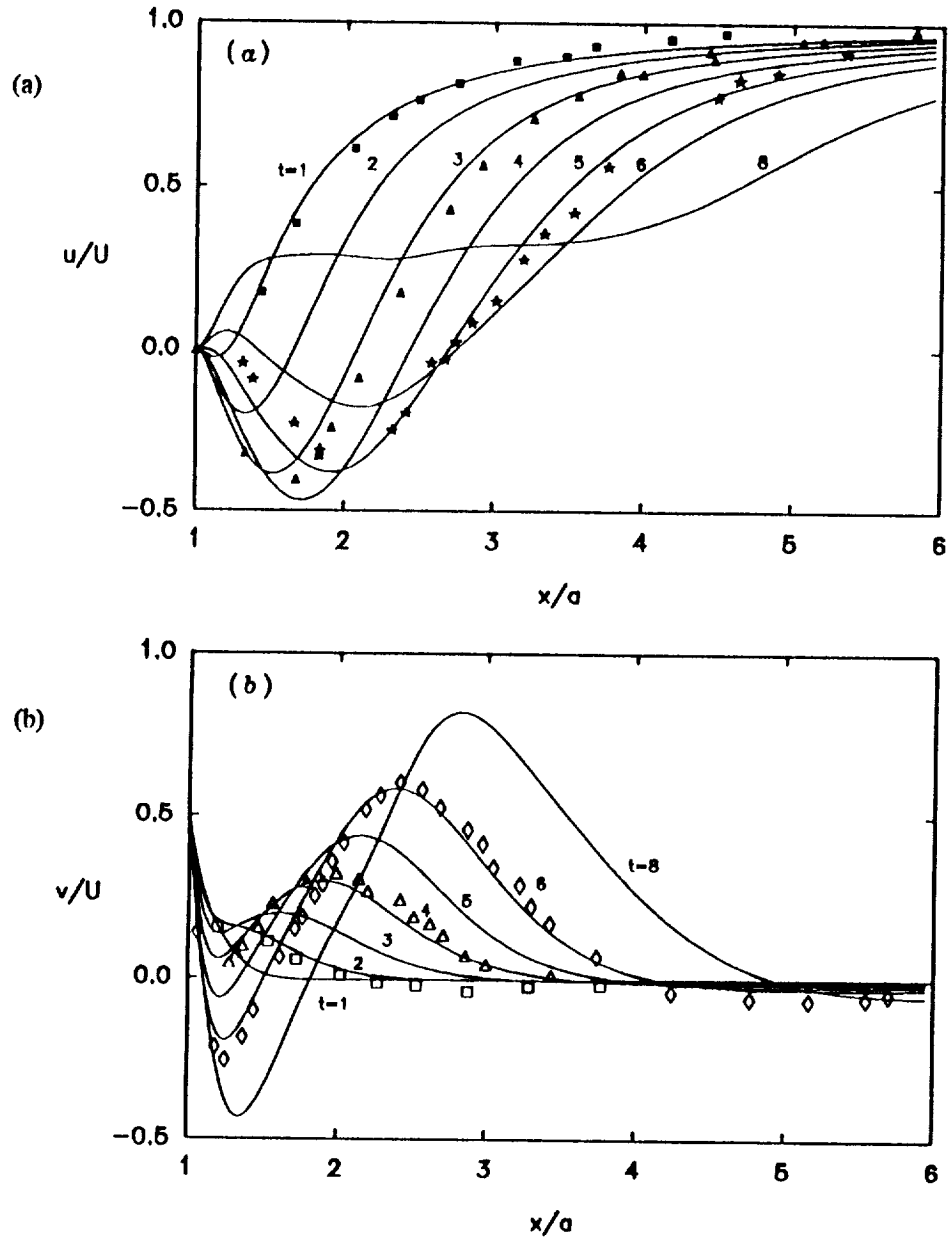
FIGURE 9. Temporal evolution of velocity profiles along the x-axis in the wake of the cylinder for $Re = 200$, $\alpha = 0.5$. ————— : numerical solution; symbols: experimental data of Coutanceau & Ménard (1985). (a) u-component, ■, $t = 1.0$; ▲, $t = 3.0$; ★, $t = 5.0$. (b) v-component, □, $t = 2.0$; △, $t = 4.0$; ◇, $t = 6.0$.

44
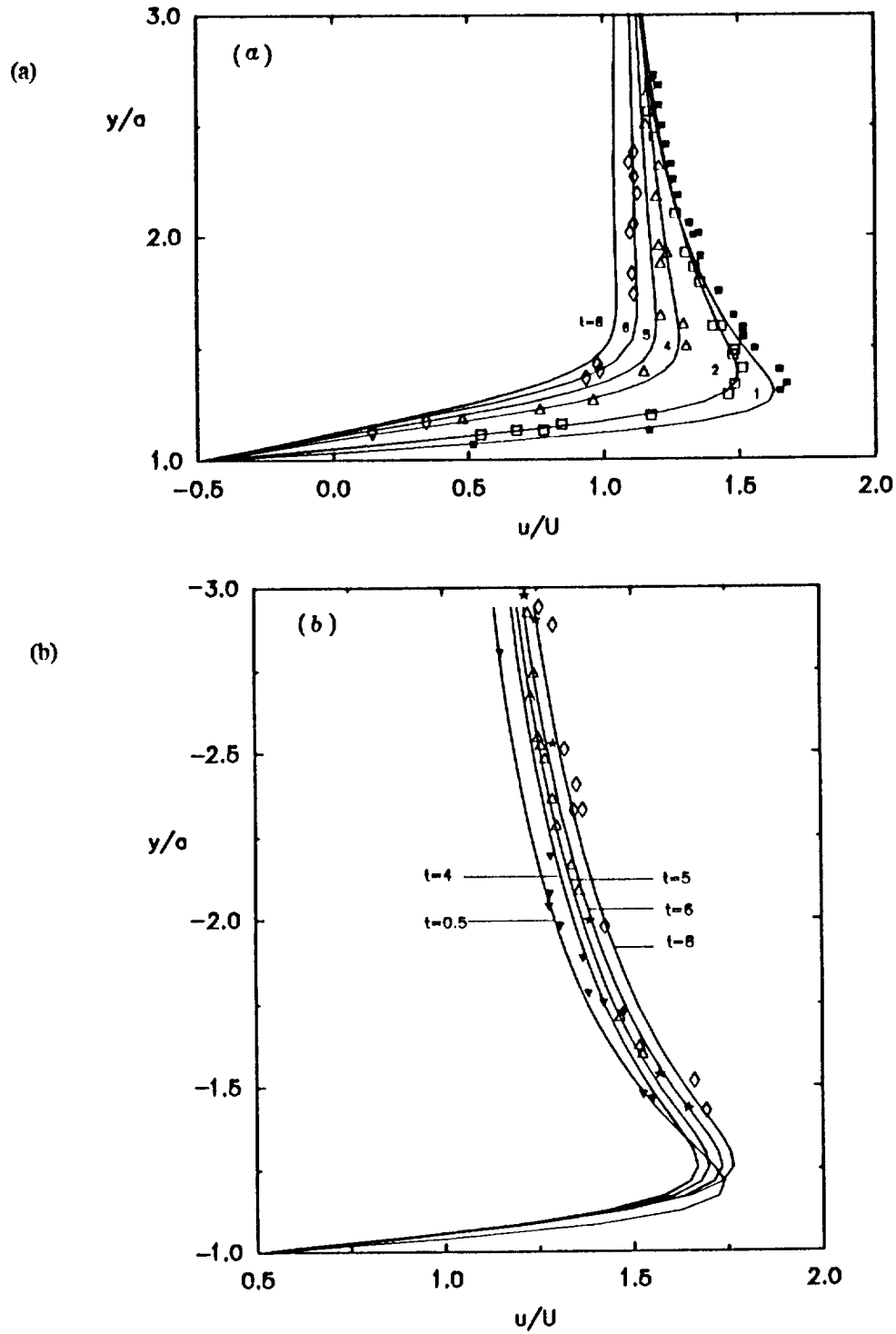
FIGURE 10. Temporal evolution of u-velocity profiles along the y-axis for $Re = 200$, $\alpha = 0.5$. ———— : numerical solution; symbols: experimental data of Coutanceau & Ménard (1985). (a) $\theta = 90°$, ■, t = 1.0; □, t = 2.0; △, t = 4.0; ◇, t = 6.0. (b) $\theta = 270°$, ▼, t = 0.5; △, t = 4.0; ★, t = 5.0; ◇, t = 6.0.

(b)

(d)

(a)

(c)

E'_3

E_2
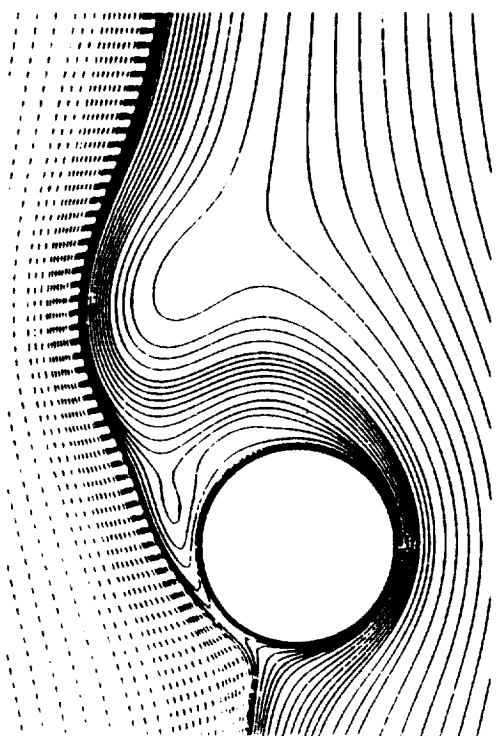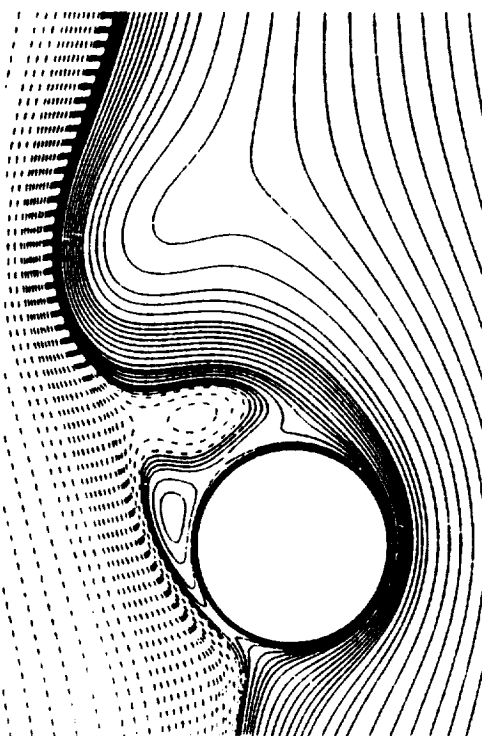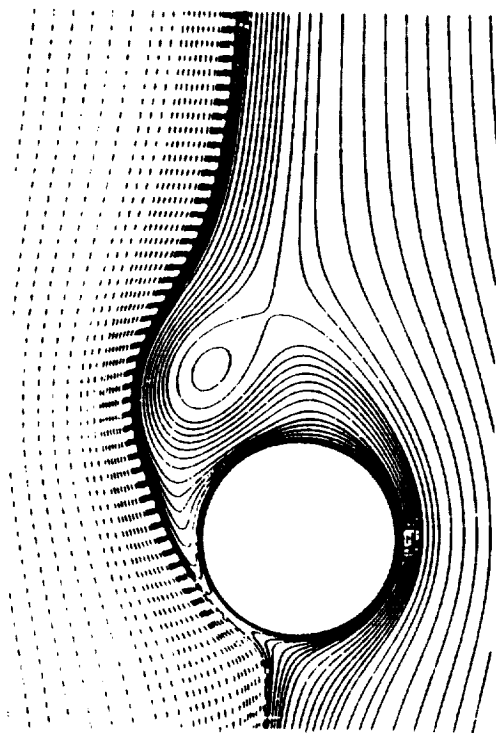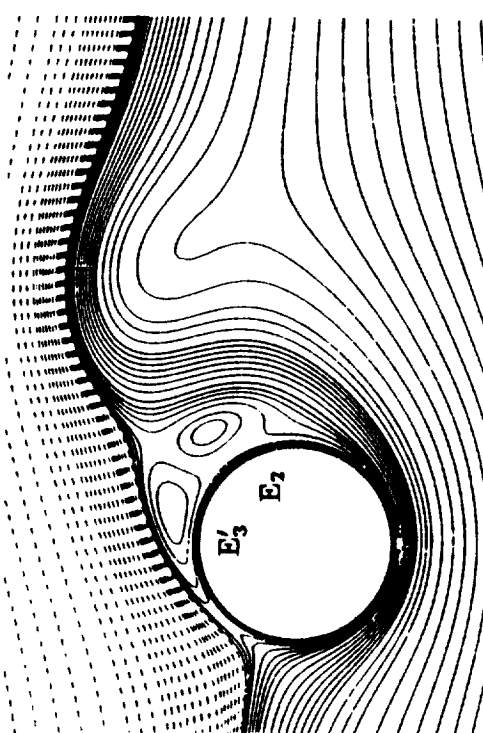
FIGURE 11 (a-d). For caption see page 48

46

(e)

(f)

(g)

(h)
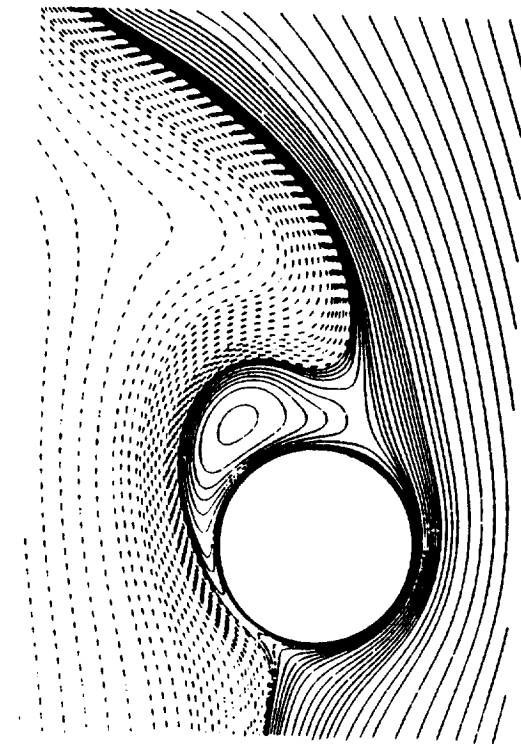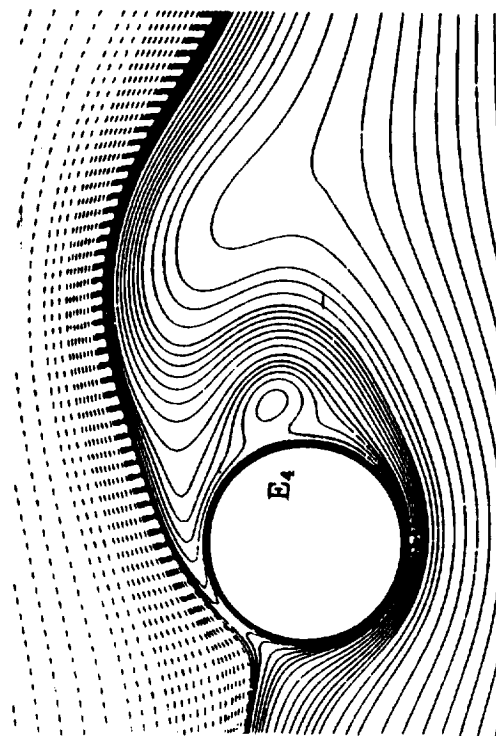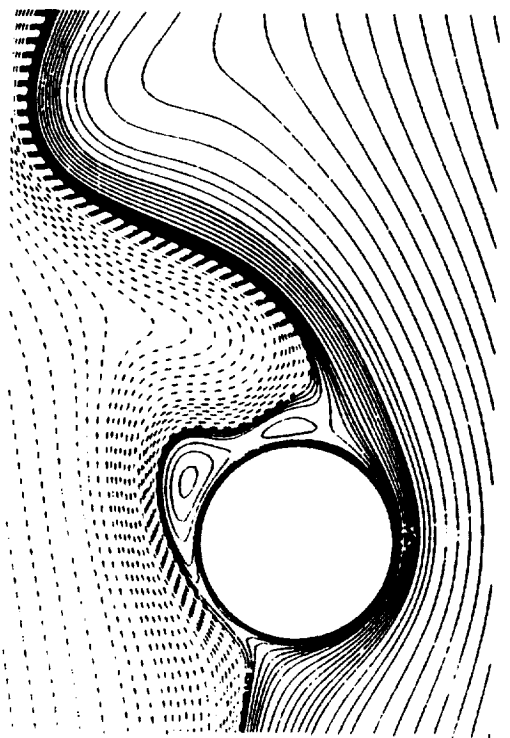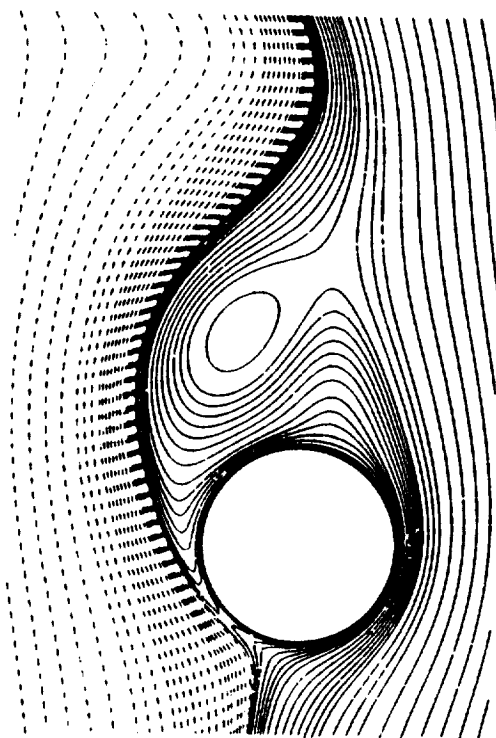
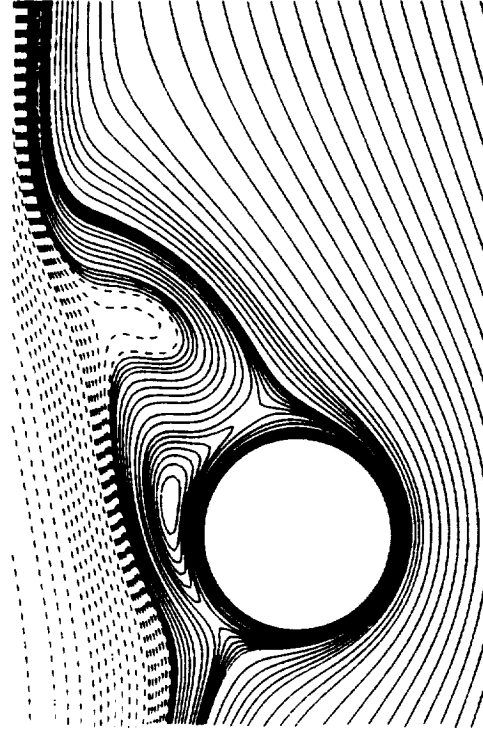FIGURE 11 (e-h). For caption see page 48

47

(j)

(i)

(l)

(k)

48
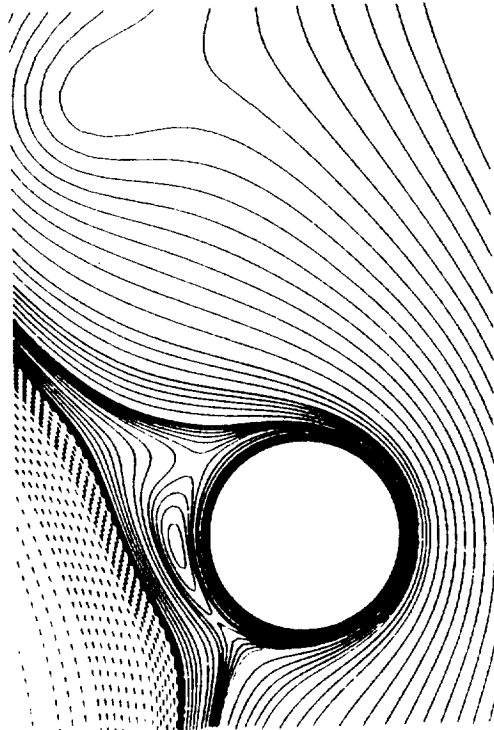
FIGURE 11. Instantaneous streamlines for $Re = 200$, $\alpha = 1.0$ at various times, viewed from the reference frame in figure 1. The plotting convention and the streamfunction values are as in figure 3. (a) $t = 4.0$, (b) $t = 6.0$, (c) $t = 6.5$, (d) $t = 7.0$, (e) $t = 9.0$, (f) $t = 11.0$, (g) $t = 14.0$, (h) $t = 16.5$, (i) $t = 17.5$, (j) $t = 18.0$, (k) $t = 21.0$, (l) $t = 24.0$.
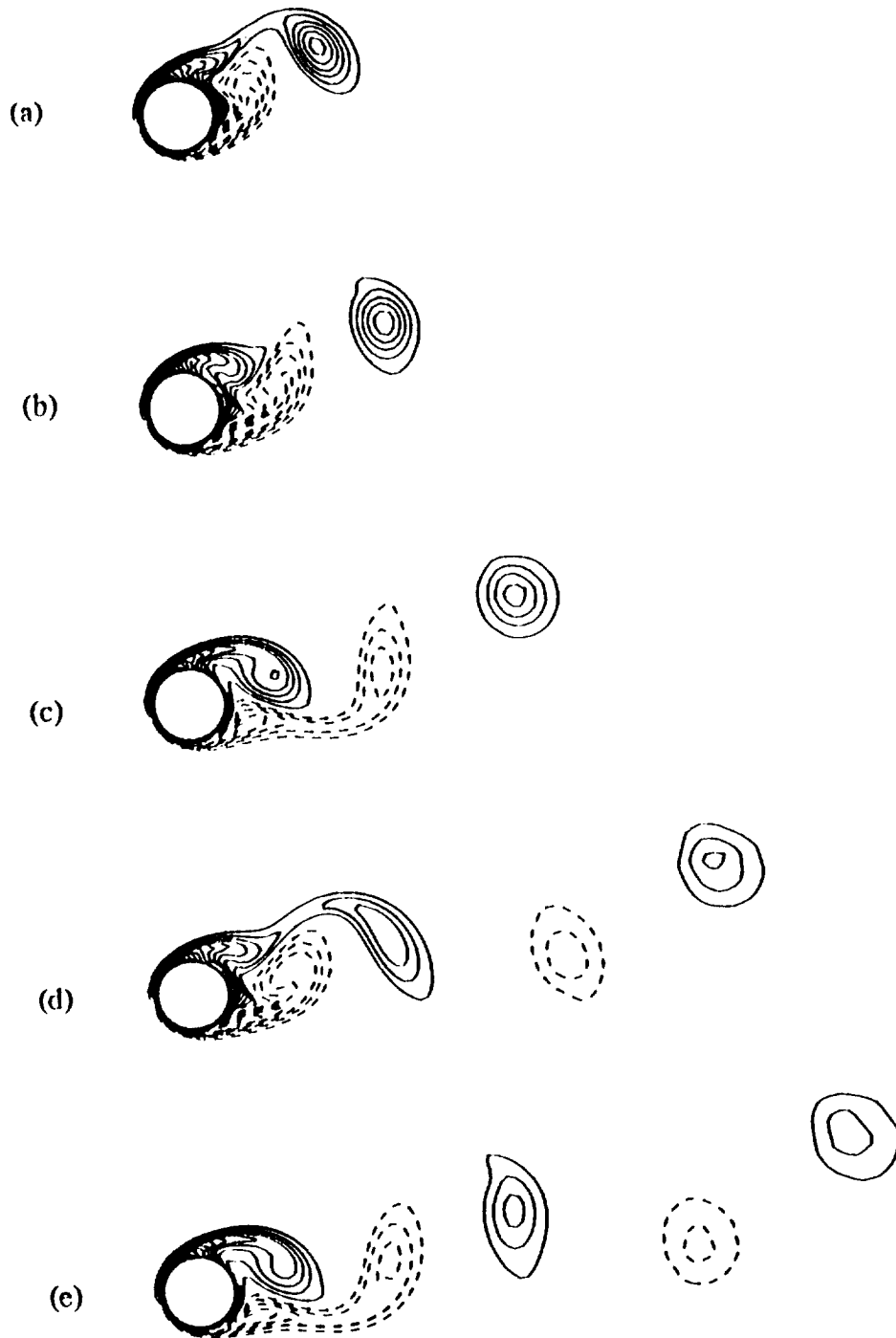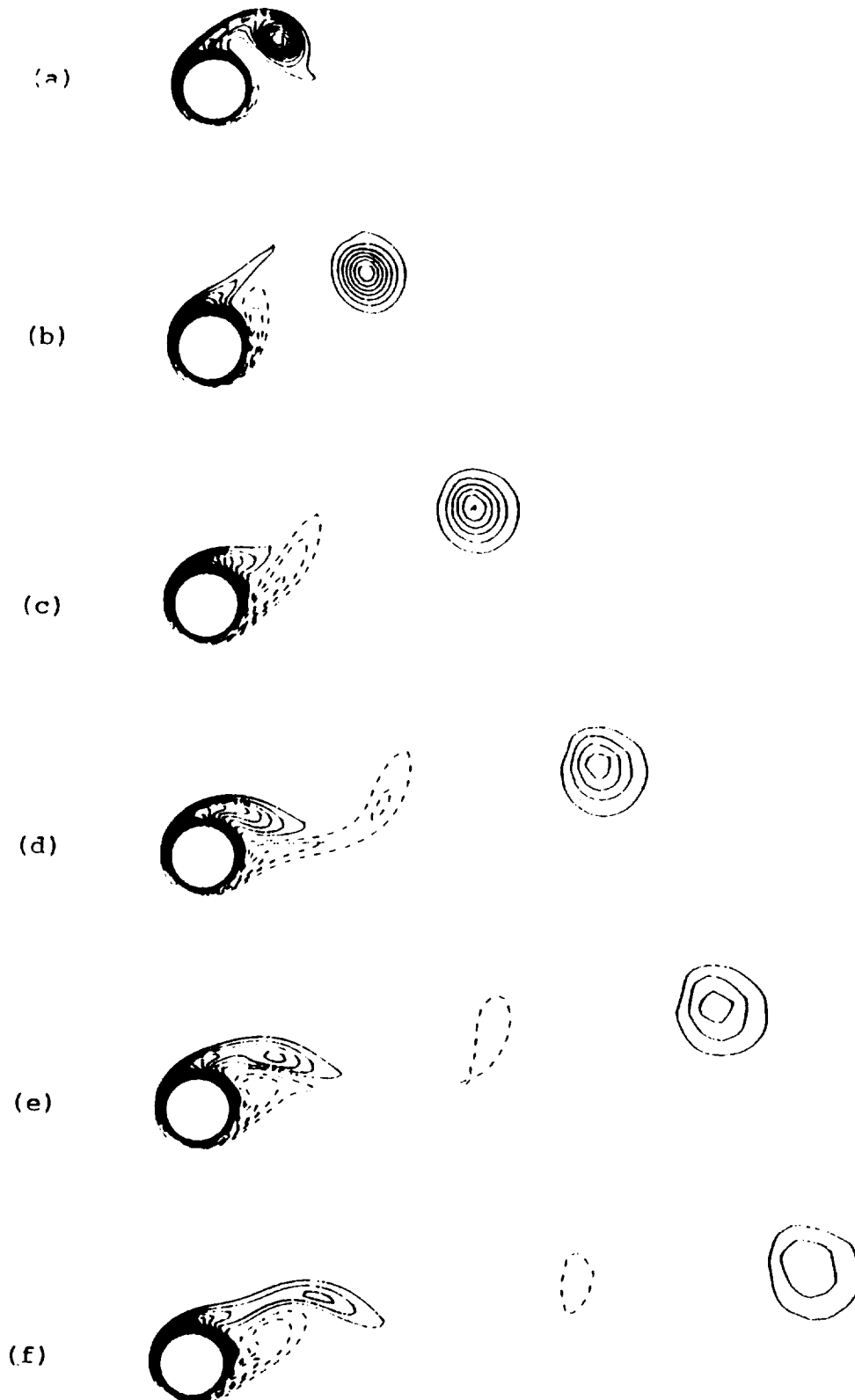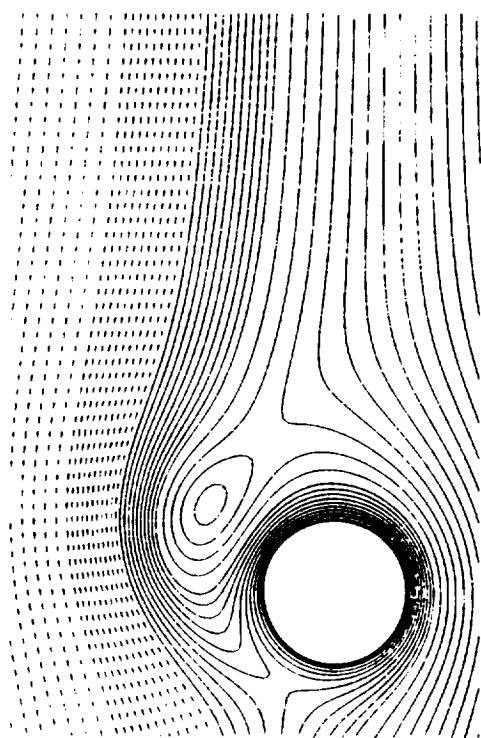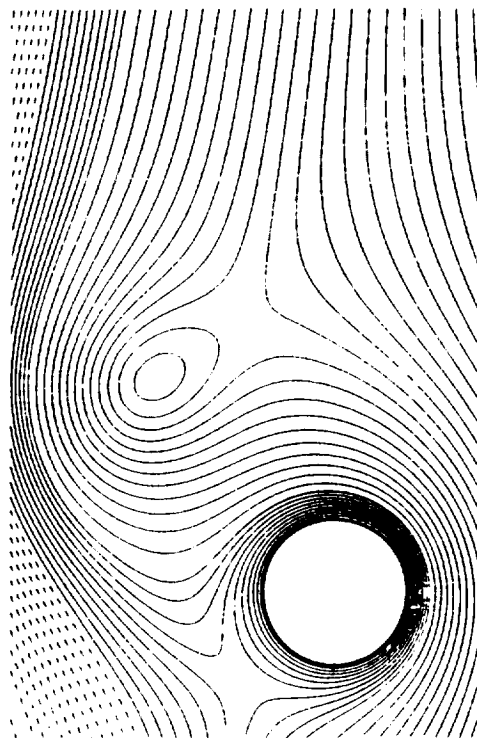
FIGURE 12. Equi-vorticity contours for $Re = 200$, $\alpha = 1.0$. Dashed (solid) lines represent constant positive (negative) vorticity values with a constant increment of 0.5. Vorticity contours with magnitude less than 0.5 are omitted for graphical clarity. (a) $t = 8.0$, (b) $t = 10.0$, (c) $t = 14.0$, (d) $t = 20.0$, (e) $t = 24.0$.
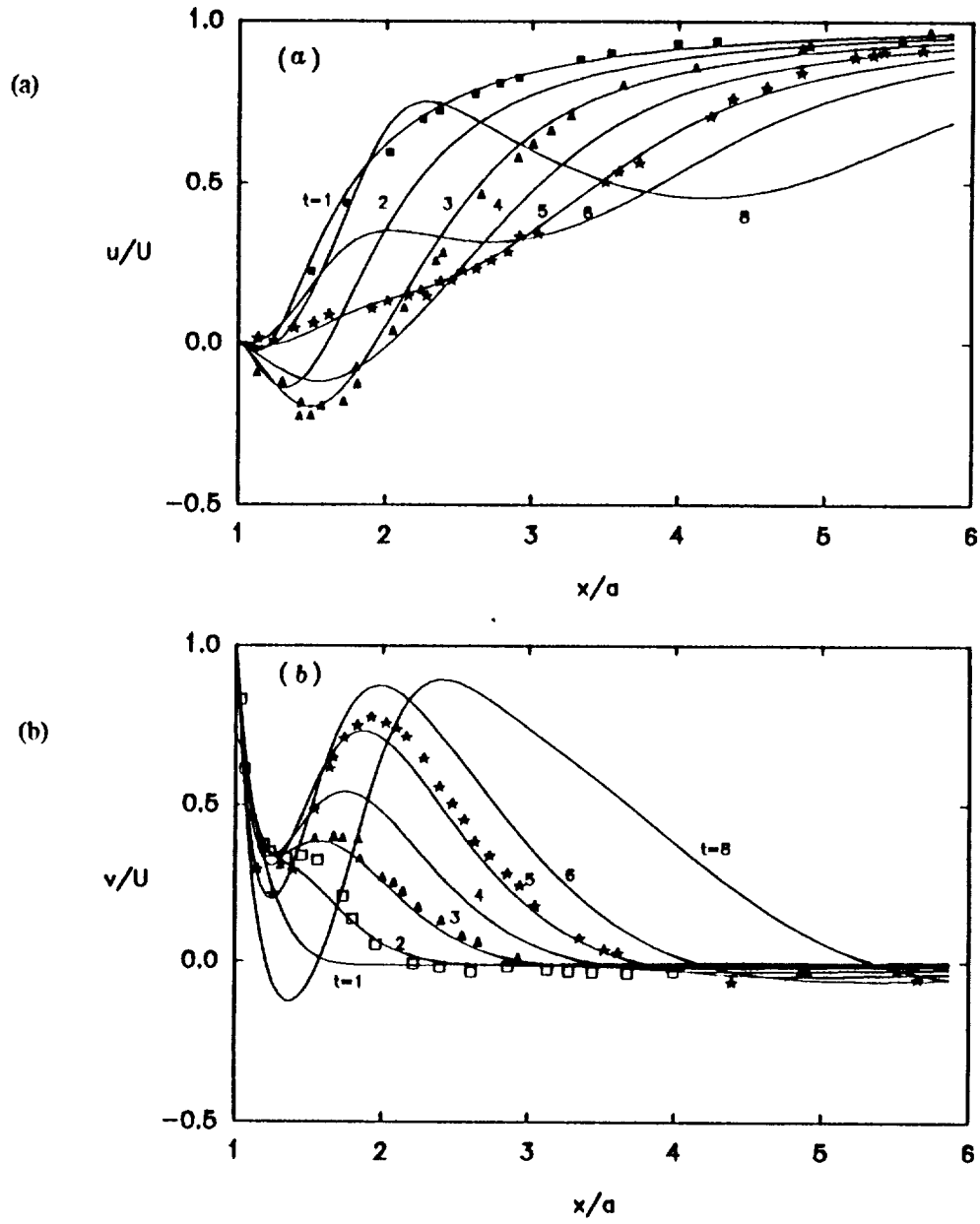
FIGURE 13. Temporal evolution of velocity profiles along the x-axis in the wake of the cylinder for $Re = 200$, $\alpha = 1.0$. ————— : numerical solution; symbols: experimental data of Coutanceau & Ménard (1985). (a) u-component, ■, $t = 1.0$; ▲, $t = 3.0$; ★, $t = 5.0$. (b) v-component, □, $t = 2.0$; ▲, $t = 3.0$; ★, $t = 5.0$.

(a)

(b)

(c)

(d)
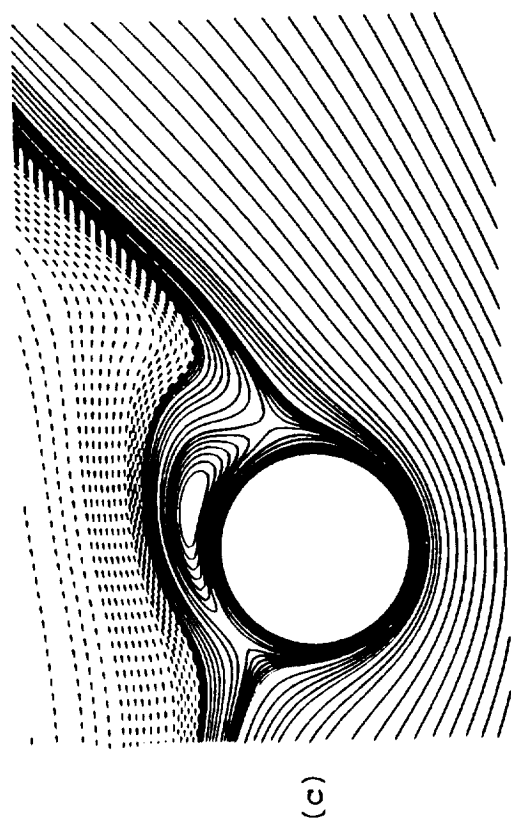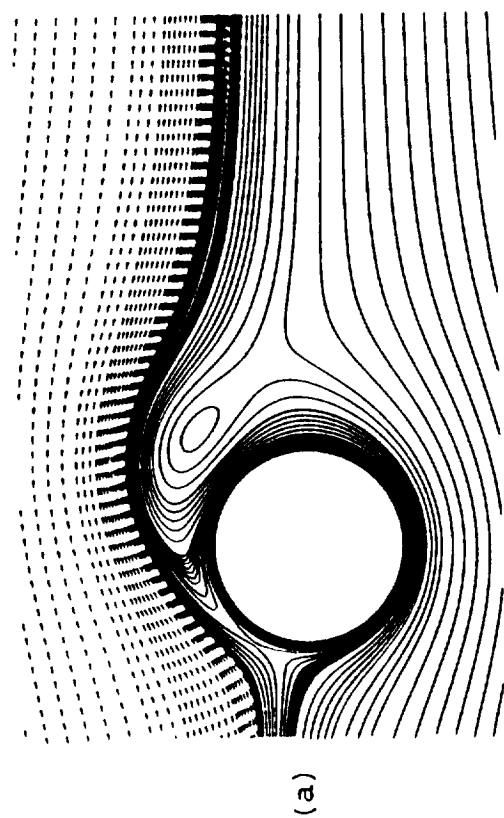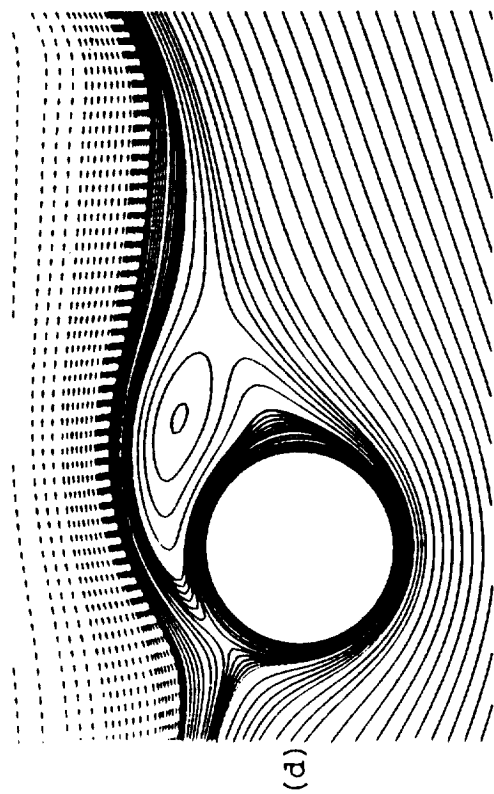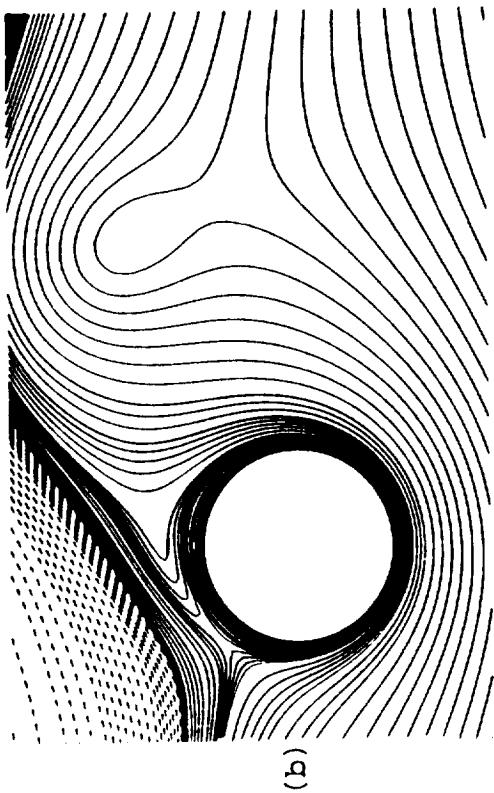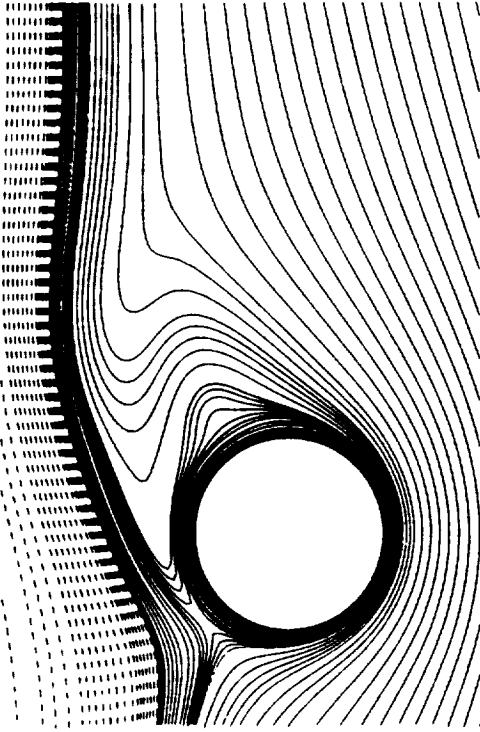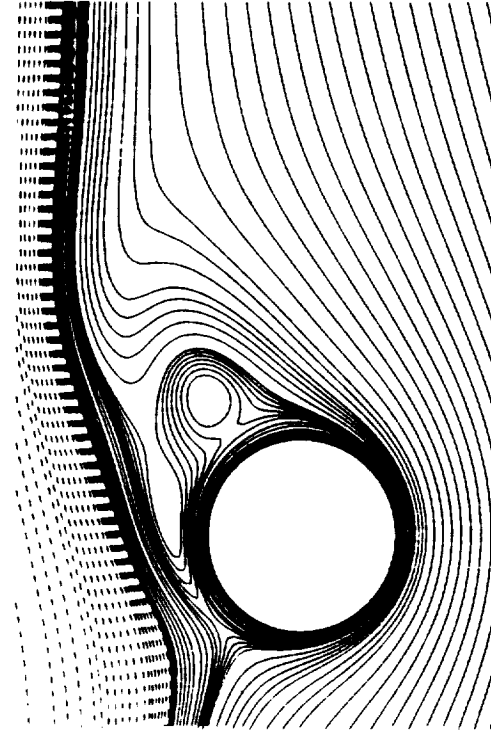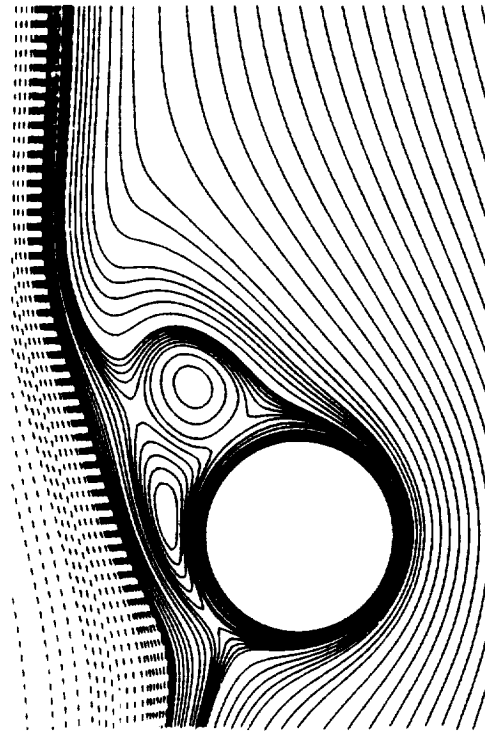
FIGURE 14. Instantaneous streamlines for $Re = 200$, $\alpha = 2.07$ at various times, viewed from the reference frame in figure 1. In addition to those given in figure 3, $\psi = -0.17$, -0.19, -0.21, -0.22, -0.23, -0.24 are also plotted. (a) $t = 3.0$, (b) $t = 7.0$, (c) $t = 13.0$, (d) $t = 17.0$, (e) $t = 21.0$, (f) $t = 22.0$, (g) $t = 22.5$, (h) $t = 24.0$.
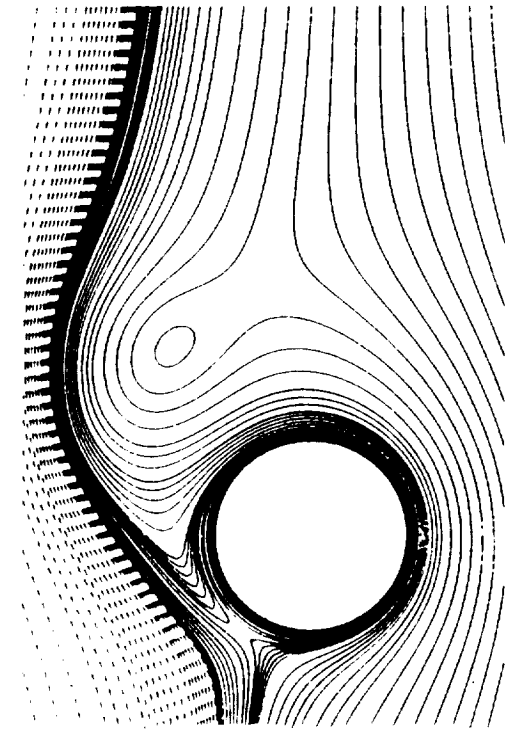
FIGURE 15. Comparison of calculated (left) and experimental (right) instantaneous streamlines for $Re = 200$, $\alpha = 2.07$. (a) $t = 5.0$, (b) $t = 9.0$.
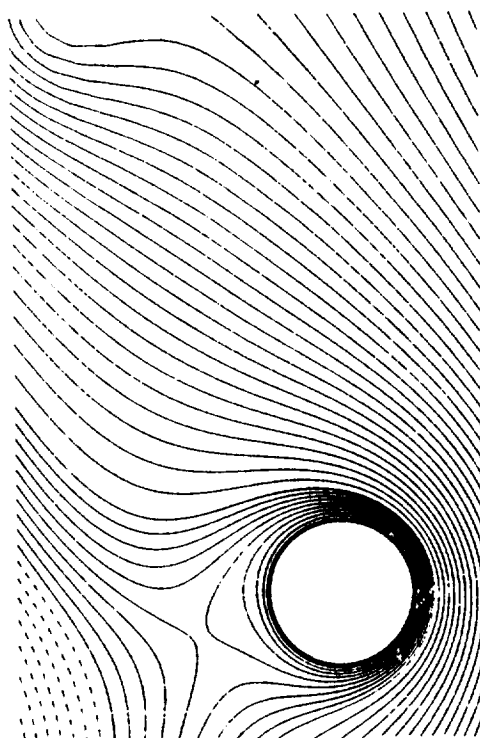
(a)

(b)

FIGURE 16. Equi-vorticity contours for $Re = 200$, $\alpha = 2.07$. Dashed (solid) lines represent constant positive (negative) vorticity values with a constant increment of 0.5. Vorticity contours with magnitude less than 0.5 are omitted for graphical clarity. (a) $t = 5.0$, (b) $t = 9.0$, (c) $t = 13.0$, (d) $t = 17.0$, (e) $t = 21.0$, (f) $t = 24.0$.
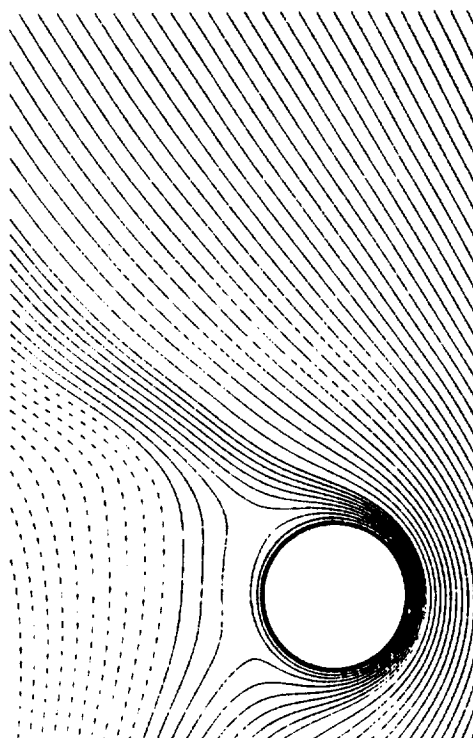
(a)

(b)

(c)

(d)

FIGURE 17. Instantaneous streamlines for $Re = 200$, $\alpha = 3.25$ at various times, viewed from the reference frame in figure 1. The plotting convention is as in figure 3. The values of ψ plotted are 0.0, ± 0.1, ± 0.2, ± 0.3, ± 0.4, ± 0.5, ± 0.6, ± 0.7, ± 0.8, ± 0.9, ± 1.0 and an increment of ± 0.2 thereafter. (a) $t = 5.0$, (b) $t = 9.0$, (c) $t = 16.0$, (d) $t = 24.0$.
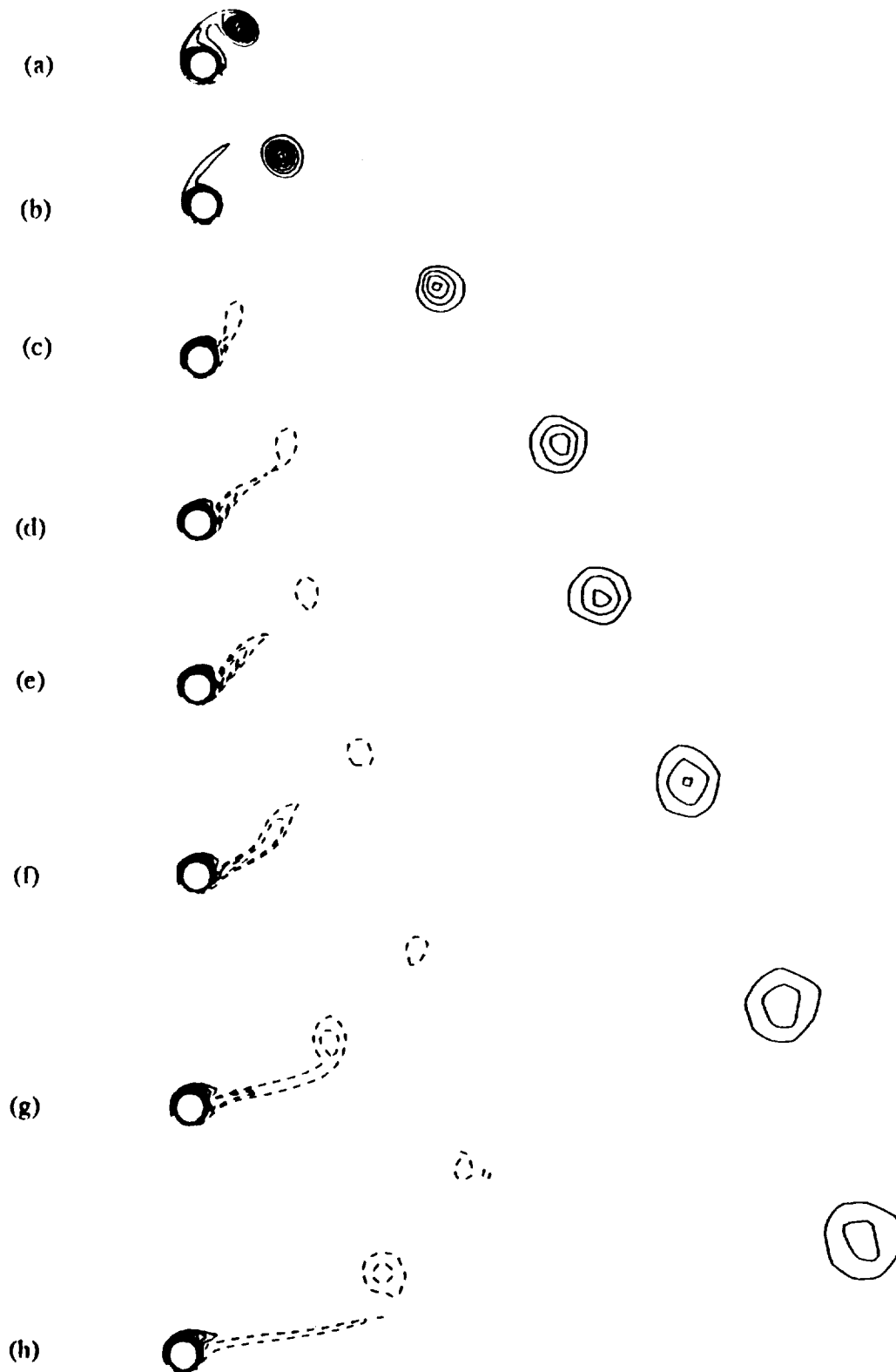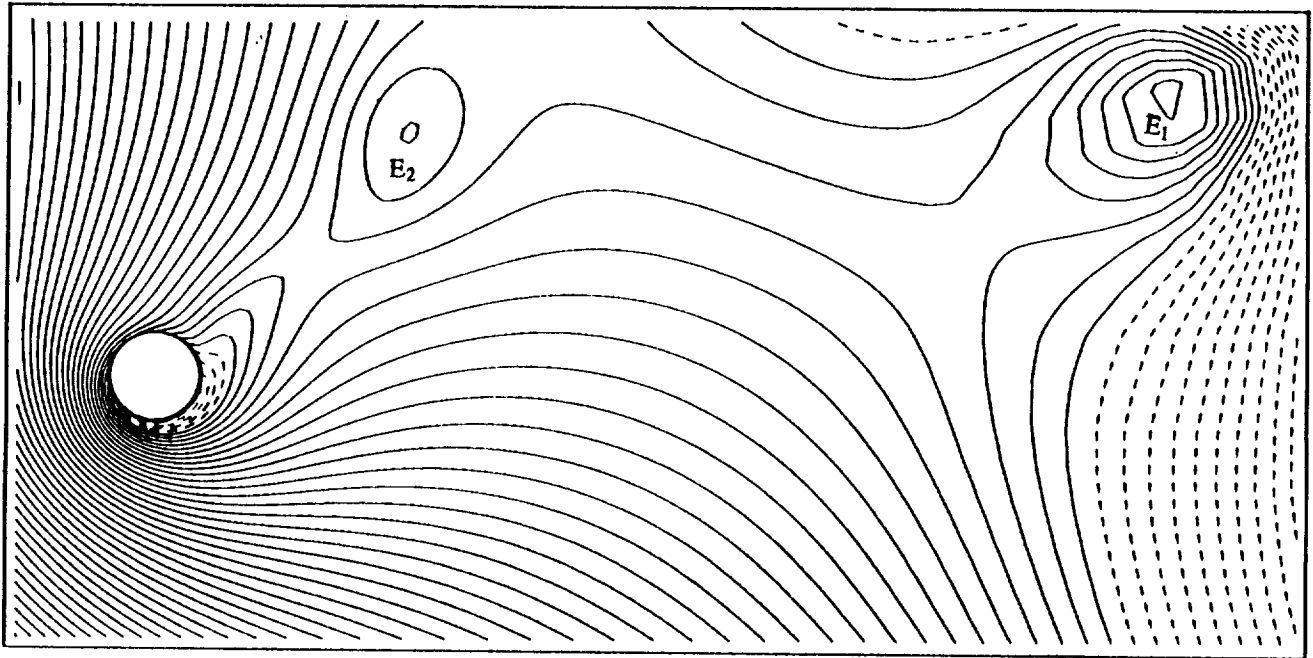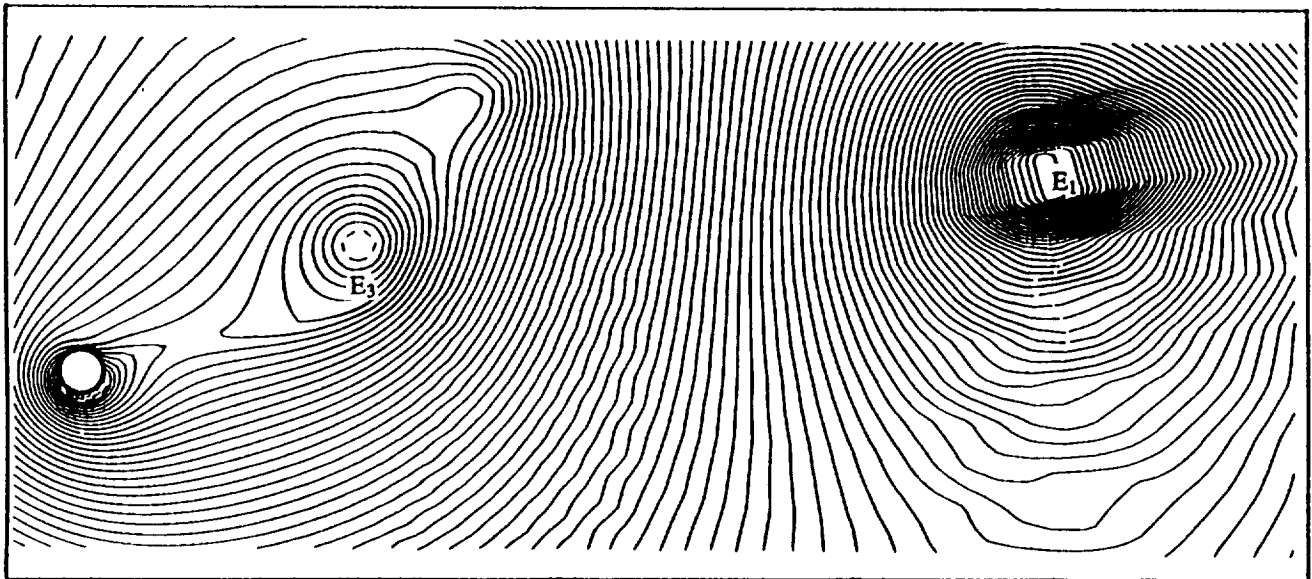
FIGURE 18. Equi-vorticity contours for $Re = 200$, $\alpha = 3.25$. Dashed (solid) lines represent constant positive (negative) vorticity values with a constant increment of 0.5. Vorticity contours with magnitude less than 0.5 are omitted for graphical clarity. (a) $t = 8.0$, (b) $t = 12.0$, (c) $t = 24.0$, (d) $t = 32.0$, (e) $t = 35.0$, (f) $t = 41.0$, (g) $t = 48.0$, (h) $t = 54.0$.

(a)

(b)

FIGURE 19. Instantaneous streamlines for $Re = 200$, $\alpha = 3.25$, (a) viewed from a frame moving with the core of the second vortex ($t = 32.0$). (b) viewed from a frame moving with the core of the third vortex ($t = 54.0$). Dashed (solid) lines represent constant positive (negative) streamfunction values with $\Delta\psi = 0.2$. Note that in (b), eddy E_2 has passed from the field of view.
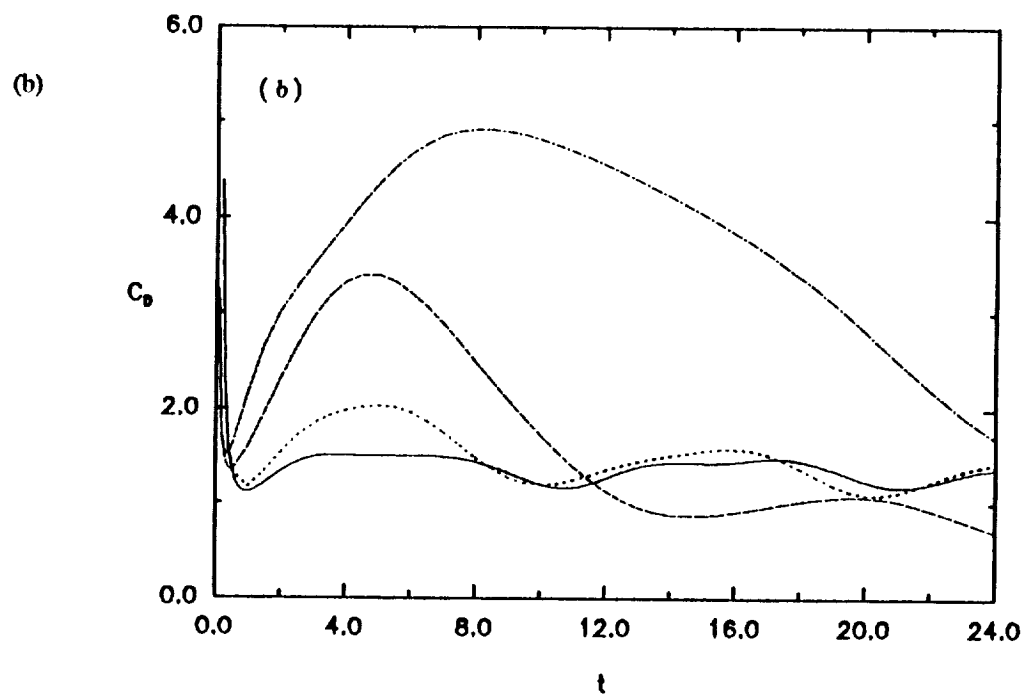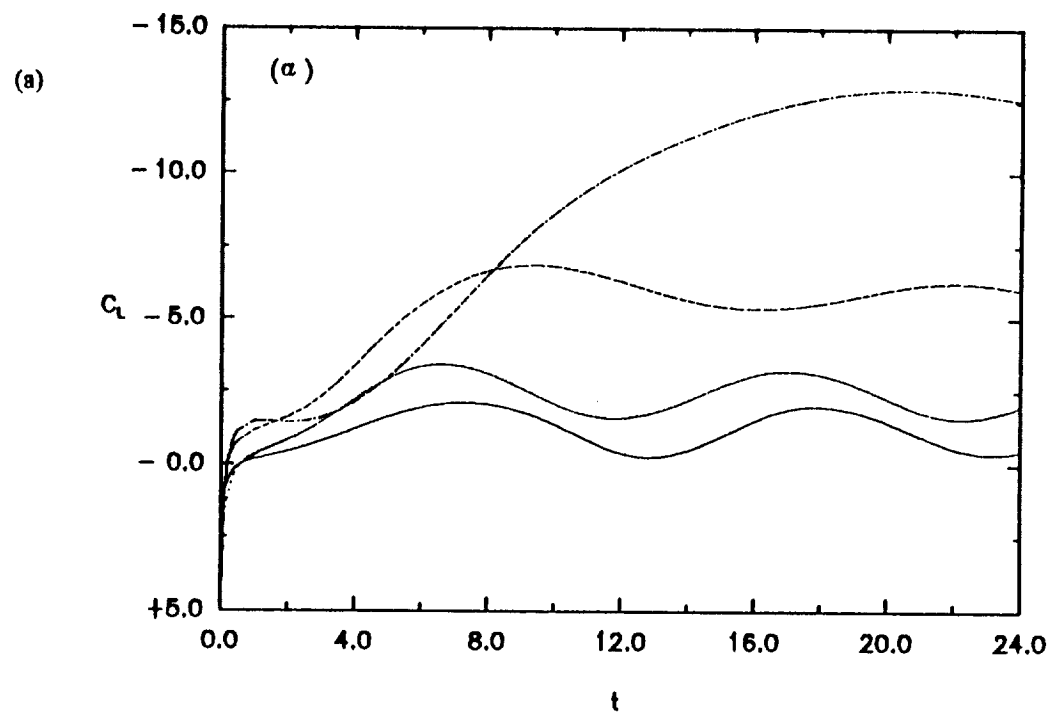
FIGURE 20. Temporal evolution of the lift (a) and drag (b) coefficients at various α up to $t = 24.0$.
——— : $\alpha = 0.5$; ······ : $\alpha = 1.0$; – – – – – : $\alpha = 2.07$; – · – · : $\alpha = 3.25$.
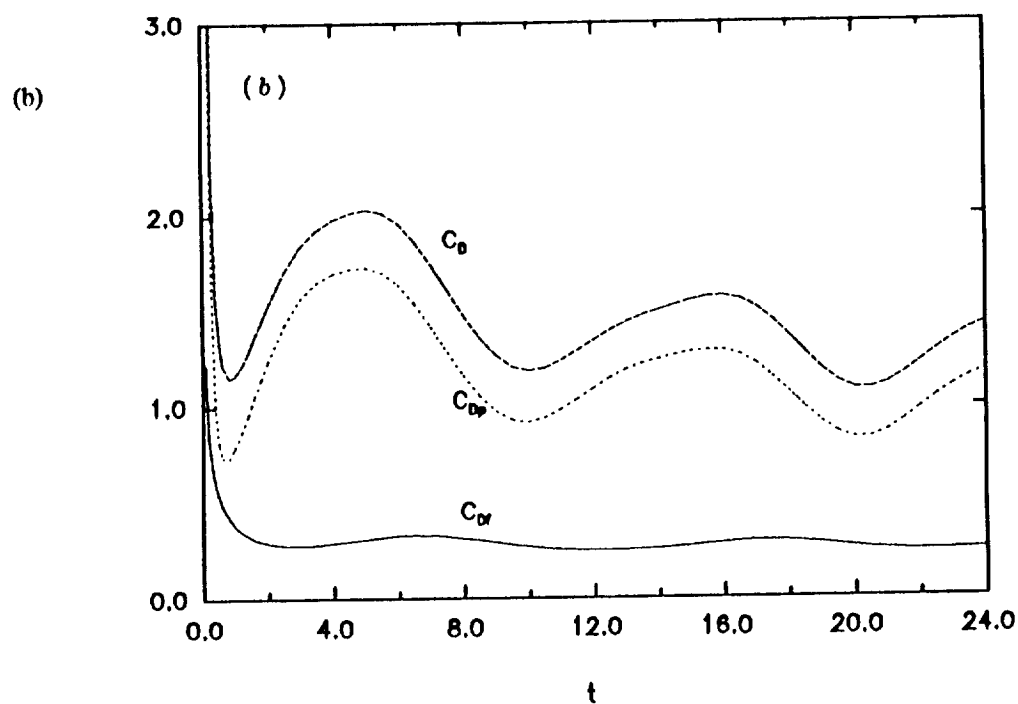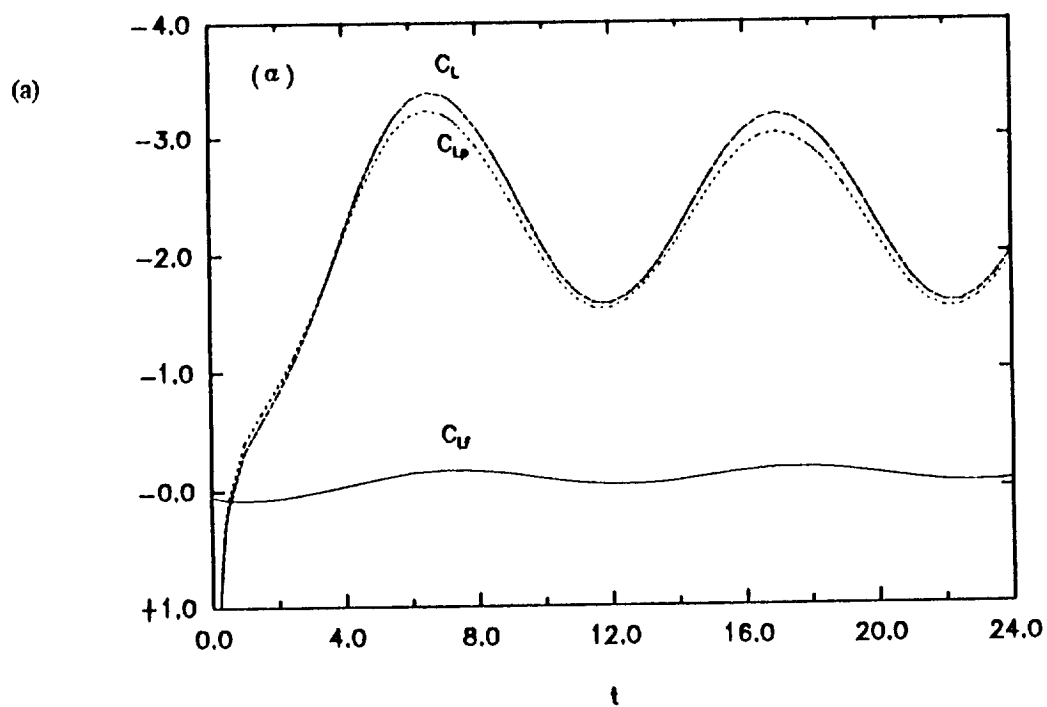
FIGURE 21. Contributions of pressure and skin friction to the lift (a) and drag (b) for $\alpha = 1.0$.
————— : skin friction; · · · · · · : pressure; — — — — : total.

1. Report No. NASA CR-187512 ICASE Report No. 91-10	2. Government Accession No.	3. Recipient's Catalog No.
4. Title and Subtitle DEVELOPMENT OF THE WAKE BEHIND A CIRCULAR CYLINDER IMPULSIVELY STARTED INTO ROTATORY AND RECTILINEAR MOTION: INTERMEDIATE ROTATION RATES		5. Report Date January 1991
		6. Performing Organization Code
7. Author(s) Yen-Ming Chen Yuh-Roung Ou Arne J. Pearlstein		8. Performing Organization Report No. 91-10
		10. Work Unit No. 505-90-52-01
9. Performing Organization Name and Address Institute for Computer Applications in Science and Engineering Mail Stop 132C, NASA Langley Research Center Hampton, VA 23665-5225		11. Contract or Grant No. NAS1-18605
12. Sponsoring Agency Name and Address National Aeronautics and Space Administration Langley Research Center Hampton, VA 23665-5225		13. Type of Report and Period Covered Contractor Report
		14. Sponsoring Agency Code

15. Supplementary Notes

16. Abstract

The temporal development of two-dimensional viscous incompressible flow generated by a circular cylinder started impulsively into steady rotatory and rectilinear motion is studied by integration of a velocity/vorticity formulation of the governing equations, using an explicit finite-difference/ pseudo-spectral technique and a new implementation of the Biot-Savart law. Results are presented for a Reynolds number of 200 (based on the cylinder diameter $2a$ and the magnitude U of the rectilinear velocity) for several values of the angular/rectilinear speed ratio $\alpha = \Omega a/U$ (where Ω is the angular speed) up to 3.25. For values of $\alpha \le 1$, our extension of the computations to larger dimensionless times than those possible in the experimental work of Coutanceau & Menard (1985) or considered in the computational work of Badr & Dennis (1985) allows for a more complete discussion of the long-term development of the wake. We also discuss several aspects of the kinematics and dynamics of the flow not considered earlier. For higher values of α, our results indicate that for Re = 200, vortex shedding does indeed occur for $\alpha = 3.25$ (and possibly for higher values of α also), in contrast to the conclusion of Coutanceau & Menard (1985). The shedding process is, however, very different from that which gives rise to the usual Karman vortex street for $\alpha = 0$. In particular, consecutive vortices shed by the body can be shed from the same side, and be of the same sense, in contrast to the nonrotating case, in which mirror-image vortices of opposite sense are shed alternately on opposite sides of the body. The implications of the results are discussed in relation to the possibility of suppressing vortex shedding by open- or closed-loop control of the rotation rate.

17. Key Words (Suggested by Author(s)) viscous incompressible flow, Kármán vortex street	18. Distribution Statement 02 - Aerodynamics 34- Fluid Mechanics and Heat Transfer Unclassified - Unlimited		
19. Security Classif. (of this report) Unclassified	20. Security Classif. (of this page) Unclassified	21. No. of pages 61	22. Price A04